PROCEEDINGS A

royalsocietypublishing.org/journal/rspa

Research

Cite this article: Li M, Kaszás B, Haller G. 2024 Variational construction of tubular and toroidal streamsurfaces for flow visualization. *Proc. R. Soc. A* **480**: 20230951. https://doi.org/10.1098/rspa.2023.0951

Received: 22 December 2023
Accepted: 25 January 2024

Subject Areas:
fluid mechanics

Keywords:
first integral, coherent structures, finite-element methods

Author for correspondence:
Mingwu Li
e-mail: limw@sustech.edu.cn

Variational construction of tubular and toroidal streamsurfaces for flow visualization

Mingwu Li[1], Bálint Kaszás[2] and George Haller[2]

[1]Department of Mechanics and Aerospace Engineering, Southern University of Science and Technology, Shenzhen 518055, People's Republic of China
[2]Institute for Mechanical Systems, ETH Zürich Leonhardstrasse 21, Zürich 8092, Switzerland

ML, 0000-0002-3570-6535; BK, 0000-0002-2024-9079; GH, 0000-0003-1260-877X

Approximate streamsurfaces of a three-dimensional velocity field have recently been constructed as isosurfaces of the closest first integral of the velocity field. Such approximate streamsurfaces enable effective and efficient visualization of vortical regions in three-dimensional flows. Here we propose a variational construction of these approximate streamsurfaces to remove the limitation of Fourier series representation of the first integral in earlier work. Specifically, we use finite-element methods to solve a partial differential equation that describes the best approximate first integral for a given velocity field. We use several examples to demonstrate the power of our approach for three-dimensional flows in domains with arbitrary geometries and boundary conditions. These include generalized axisymmetric flows in the domains of a sphere (spherical vortex), a cylinder (cylindrical vortex) and a hollow cylinder (Taylor–Couette flow) as benchmark studies for various computational domains, non-integrable periodic flows (ABC and Euler flows) and Rayleigh–Bénard convection flows. We also illustrate the use of the variational construction in extracting momentum barriers in Rayleigh–Bénard convection.

1. Introduction

Streamlines provide a powerful tool for the visualization of two-dimensional flows but have limited usefulness for three-dimensional flows [1]. Indeed, a streamline

THE ROYAL SOCIETY PUBLISHING

passes through every point of a flow and hence one needs to select a few illustrative streamlines to provide an efficient visualization [2,3].

As an alternative, streamsurfaces are well-known techniques for the visualization of three-dimensional flows. As in the case of streamlines, one has to find a select set of special streamsurfaces that efficiently convey information about the range of different fluid behaviours in the flow domain. This is not an easy task, given that infinitely many streamsurfaces pass through each point of the flow domain.

Hultquist [4] proposed an advancing front method to construct streamsurfaces. With a properly chosen curve, this is discretized with a set of particles and then advanced downstream. In particular, the spacing between particles at the front and the number of these particles are adaptively changed such that the distance between two adjacent particles is kept the same. This method highly depends on the initial curve and requires a careful implementation [1].

The stream function ϕ of any two-dimensional, incompressible flow is guaranteed to exist and can be used to visualize the streamlines for the two-dimensional flow because the contour lines of this function ϕ are the streamlines. Motivated by this observation, van Wijk [1] seeks a scalar function f such that $f(\mathbf{x}) = C$ represents a one-parameter family of streamsurfaces for a given three-dimensional flow under the variations in C. To solve for the function f, a convection equation is used and then simulated with prescribed values of f at boundaries [1]. This simulation is performed until a steady state is reached. A similar approach is proposed to define vortex surfaces where the local vorticity vector is tangent at every point on such a surface [5]. Similarly, one can simulate the convection equation to solve for the scalar function f whose contour plots give the vortex surfaces [6,7].

The aforementioned simulations of the convection equation depend on the choice of the initial distribution of f, which is not trivial. In addition, long-time simulations are needed to obtain converged solutions [6]. Therefore, simulating the associated convection equation remains challenging and computationally expensive.

By definition, the scalar function f is a first integral for three-dimensional steady flows or unsteady flows that are instantaneously frozen. However, an exact first integral does not exist for generic three-dimensional flows. Some exceptions include the Bernoulli function, which gives a non-degenerate first integral for steady Euler flows that do not satisfy the Beltrami property [8]. Analytic first integrals were also constructed for incompressible flows with a volume-preserving symmetry group [9] and for highly symmetric flows [10].

Although for a typical three-dimensional flow, exact first integrals do not exist, approximate first integrals can be found in vortical regions of the flow. As argued by Katsanoulis *et al*. [11], vortical regions contain either two-dimensional tubes or tori and form Cantor sets in the three-dimensional phase space [12]. Motivated by the fact that Hamiltonian systems become integrable when restricted to those Cantor sets [13], we seek smooth functions that act as approximate first integrals over the Cantor family of tori but not in the gaps between them.

A level surface of a first integral, $f = C$, is also an invariant manifold. Such manifolds have been broadly used to illustrate local velocity geometry near stationary points [14]. However, these invariant manifolds generally stretch and fold globally, which makes them unsuitable for global flow visualization. Exceptions to this general rule are invariant manifolds that are level surfaces of a smooth function.

Motivated by the above observations, Katsanoulis *et al.* [11] seek influential streamsurfaces as level sets of approximate first integrals. In particular, they constructed a scalar function f to minimize $|\nabla f \cdot \mathbf{v}|$ at a collection of grid points [11]. Here $\mathbf{v}$ can be a general vector field related to the fluid motion, such as the velocity, vorticity or even a barrier field used for detecting barriers to material transport [15]. These barrier fields have been introduced to define material sets that prohibit the transport of active quantities in a frame-indifferent way. For example, the method was used to extract objective momentum barriers as invariant manifolds of the barrier vector fields defined in [15,16].

Katsanoulis *et al.* [11] use a Fourier series to represent the unknown scalar function f. This approach works well for spatially periodic flows but has limitations for generic flows that are

not periodic in all three directions. Although such spatially aperiodic flows have also been successfully treated via a proper choice of smaller subdomains, the selection of such subdomains is problem-dependent and hence requires careful implementation.

To extend the approximate first integral approach of Katsanoulis *et al.* [11] to generic three-dimensional flows, here we develop a variational construction of approximate first integrals for three-dimensional velocity fields given by either analytic expressions or datasets. This variational approach works for arbitrary geometries and boundary conditions of the computational domain. The approximate first integrals here are obtained as eigenfunctions of a set of linear partial differential equations (PDEs) obtained as the Euler–Lagrange equations of the variational principle of minimizing $|\nabla f \cdot \mathbf{v}|$. We use finite-element methods to discretize the PDEs and then solve for the eigenvectors corresponding to the smallest eigenvalues. These eigenvectors provide the approximate first integrals of the three-dimensional flow.

The remainder of this paper is organized as follows. We start with a formulation of an optimization problem whose solution gives the approximate first integrals. We derive the first-order necessary conditions of the optimization problem in §2, which are the aforementioned PDEs. Then we establish the weak form of the PDEs in §3, which leads to an eigenvalue problem. In §4, we discuss the relation between the solutions of this eigenvalue problem and the minimum solution of the optimization problem. The solution of the weak form via finite-element methods is then discussed in §5, followed by benchmark studies on three-dimensional flow in domains with arbitrary geometries in §6. We further consider periodic flows in §7 and non-periodic Rayleigh–Bénard convection flows in §8 to illustrate the broad applicability of our method.

2. Formulation

Consider a vector field $\mathbf{u} : \Omega \to \mathbb{R}^3$ defined over a spatial domain $\Omega \subset \mathbb{R}^3$. We define the function space of admissible first integrals as

$$\mathcal{H} = \left\{ H \in H^1(\Omega), \int_\Omega H^2 \, \mathrm{d}V = 1 \right\} \tag{2.1}$$

and consider the optimization problem

$$H^* = \underset{H \in \mathcal{H}}{\operatorname{argmin}} \int_\Omega ||\nabla H \cdot \mathbf{u}||^2 \, \mathrm{d}V. \tag{2.2}$$

We have introduced the normalization constraint $||H||_{L^2} = 1$ to exclude the multitude of trivial solutions $H = C$. Indeed, these are minimal solutions for any constant C. With the imposed constraint, the only constant solution remains $H = 1/\sqrt{\mathrm{Vol}(\Omega)}$, where $\mathrm{Vol}(\Omega) = \int_\Omega \mathrm{d}V$.

We introduce a Lagrange multiplier to enforce the constraint and define the Lagrangian as

$$\mathcal{L}(H) = \int_\Omega ||\nabla H \cdot \mathbf{u}||^2 \, \mathrm{d}V - \lambda \left(\int_\Omega H^2 \, \mathrm{d}V - 1 \right), \tag{2.3}$$

where λ is a Lagrange-multiplier. To express the Lagrangian in terms of the components of $\mathbf{u}$ and ∇H, we make use of the implied summation over repeated indices. The components of the gradient vector are denoted as $(\nabla H)_i = \partial_i H$, which allows us to write the Lagrangian as

$$\mathcal{L}(H) = \int_\Omega (\partial_i H u_i)^2 \, \mathrm{d}V - \lambda \left(\int_\Omega H^2 \, \mathrm{d}V - 1 \right). \tag{2.4}$$

Note that the variation of the first term in (2.4) is

$$\delta \left(\int_\Omega (\partial_i H u_i)^2 \, \mathrm{d}V \right) = 2 \int_{\partial\Omega} \partial_i H u_i u_j n_j \delta H \, \mathrm{d}S - 2 \int_\Omega \partial_j (\partial_i H u_i u_j) \delta H \, \mathrm{d}V. \tag{2.5}$$

Since the variation of the second term in (2.4) is simply $2\lambda H$, we obtain the following first-order necessary conditions for the minimum solution:

$$\partial_j (\partial_i H u_i u_j) = -\lambda H, \quad \text{on } \Omega \tag{2.6}$$

royalsocietypublishing.org/journal/rspa Proc. R. Soc. A 480: 20230951

and

$$\partial_i H u_i u_j n_j \delta H = (\nabla H \cdot \mathbf{u})(\mathbf{u} \cdot \mathbf{n})\delta H = 0, \quad \text{on } \partial\Omega, \text{ and } \int_\Omega H^2 \, \mathrm{d}V = 1. \tag{2.7}$$

This system of equations defines an eigenvalue problem. Let $\partial\Omega = \partial\Omega_H \cup \partial\Omega_F$ with $\partial\Omega_H \cap \partial\Omega_F = \emptyset$, where $\partial\Omega_H$ denotes the part of the boundary where H is prescribed. So the boundary conditions can be further specified as

$$H(\mathbf{x}) = 0, \quad \forall \mathbf{x} \in \partial\Omega_H \quad \text{and} \quad (\nabla H \cdot \mathbf{u})(\mathbf{u} \cdot \mathbf{n}) = 0, \quad \forall \mathbf{x} \in \partial\Omega_F. \tag{2.8}$$

We have assumed homogeneous boundary conditions for $\mathbf{x} \in \partial\Omega_H$ without loss of generality, since we can add an arbitrary constant to the minimum solution and such an updated solution is still a minimum solution. Note that whenever $\partial\Omega_\mathrm{H} \neq \emptyset$ the constant solution $H = 1/\sqrt{\mathrm{Vol}(\Omega)}$ is no longer a solution to the minimization problem, since it cannot satisfy the homogeneous boundary condition.

3. Weak form

We select the trial function space $\mathcal{H}_{\text{trial}}$ for solving the eigenvalue problem (2.6) and (2.7) as

$$\mathcal{H}_{\text{trial}} = \{H \in H^1(\Omega), H(\mathbf{x}) = 0, \ \forall \mathbf{x} \in \partial\Omega_H\}. \tag{3.1}$$

We also introduce the test function space that is the same as the trial function space. To obtain the weak form of the PDE (2.6), we multiply both sides of the equation by $h \in \mathcal{H}_{\text{trial}}$ and perform integration over the domain Ω to obtain

$$\int_\Omega \partial_j(\partial_i H u_i u_j) h \, \mathrm{d}V = -\lambda \int_\Omega H h \, \mathrm{d}V. \tag{3.2}$$

For the left-hand side, we have

$$\begin{aligned}
\int_\Omega \partial_j(\partial_i H u_i u_j) h \, \mathrm{d}V &= \int_\Omega \partial_j(\partial_i H u_i u_j h) \, \mathrm{d}V - \int_\Omega \partial_i H u_i u_j \partial_j h \, \mathrm{d}V \\
&= \int_{\partial\Omega} \partial_i H u_i u_j h n_j \, \mathrm{d}S - \int_\Omega \partial_i H u_i u_j \partial_j h \, \mathrm{d}V \\
&= \int_{\partial\Omega} (\nabla H \cdot \mathbf{u})(\mathbf{u} \cdot \mathbf{n}) h \, \mathrm{d}S - \int_\Omega (\nabla H \cdot \mathbf{u})(\nabla h \cdot \mathbf{u}) \, \mathrm{d}V \\
&= -\int_\Omega (\nabla H \cdot \mathbf{u})(\nabla h \cdot \mathbf{u}) \, \mathrm{d}V := -a(H, h),
\end{aligned} \tag{3.3}$$

where we have used the facts that $h(\mathbf{x}) = 0$ for $\mathbf{x} \in \Omega_H$ and $(\nabla H \cdot \mathbf{u})(\mathbf{u} \cdot \mathbf{n}) = 0$ for $\mathbf{x} \in \Omega_F$. So the weak form is obtained as follows:

$$a(H, h) = \lambda \langle H, h \rangle, \tag{3.4}$$

where $\langle H, h \rangle = \int_\Omega H h \, \mathrm{d}V$.

4. Eigensolutions and minimum solution

Any discretization of the eigenvalue problem (2.6) and (2.7) has a set of eigensolutions $\{(H_i, \lambda_i)\}$ that satisfies

$$a(H_i, h) = \lambda_i \langle H_i, h \rangle. \tag{4.1}$$

Although we expect that the same holds true for the partial differential equations (2.6) and (2.7), this would require further analysis to establish, which we do not carry out in this paper. Since $a(\cdot, \cdot)$ is a symmetric bi-linear operator (namely, $a(H, h) = a(h, H)$), the following hold:

— The eigenvalue λ_i is real and hence H_i is also a real-valued function. To see that, we note that $a(\bar{H}_i, h) = \bar{\lambda}_i \langle \bar{H}_i, h \rangle$. It follows that

$$a(H_i, \bar{H}_i) = \lambda_i \langle H_i, \bar{H}_i \rangle \quad \text{and} \quad a(\bar{H}_i, H_i) = \bar{\lambda}_i \langle \bar{H}_i, H_i \rangle. \tag{4.2}$$

Since $a(H_i, \bar{H}_i) = a(\bar{H}_i, H_i)$ and $\langle H_i, \bar{H}_i \rangle = \langle \bar{H}_i, H_i \rangle$, we have $\lambda_i = \bar{\lambda}_i$ and hence λ_i is real.

— The eigenvalues are all non-negative, $\lambda_i \geq 0$. This follows from the fact that $a(\cdot, \cdot)$ is a positive semi-definite operator, since

$$a(H, H) = \int_\Omega |\nabla H \cdot \mathbf{u}|^2 \, \mathrm{d}V \geq 0. \tag{4.3}$$

As a result, we can arrange these eigenvalues as $0 \leq \lambda_1 \leq \lambda_2 \leq \cdots$.

— The eigenfunctions are orthogonal to each other, i.e. $\langle H_i, H_j \rangle = 0$ if $\lambda_i \neq \lambda_j$. Likewise, we have $a(H_i, H_j) = 0$ if $\lambda_i \neq \lambda_j$.

We now introduce a Rayleigh quotient

$$R(h) = a(h, h), \quad \text{with } \langle h, h \rangle = 1. \tag{4.4}$$

After the orthonormalization of $\{H_i\}$, we have $\langle H_i, H_j \rangle = \delta_{ij}$. If we let $h = \sum_i c_i H_i$, then $\langle h, h \rangle = 1$ implies that $\sum_i c_i^2 = 1$. Then the Rayleigh quotient becomes

$$R(h) = a\left(\sum_i c_i H_i, \sum_j c_j H_j \right) = \sum_i c_i^2 a(H_i, H_i) = \sum_i \lambda_i c_i^2 \geq \lambda_1. \tag{4.5}$$

The minimum is achieved when $h = H_1$. Similarly, if we restrict $c_1 = \cdots c_{i-1} = 0$, we have

$$R(h) \geq \lambda_i. \tag{4.6}$$

In the case that $\Omega_H = \emptyset$, the constant $H = 1/\mathrm{Vol}(\Omega)$ is a minimal solution, therefore we have $\lambda_1 = 0$. However, this trivial solution is not the first integral we seek. Thus, we should restrict $c_1 = 0$ and look for H_2. The eigenvalue λ_2 characterizes the minimal value of the objective functional. Note that the second eigenvalue λ_2 is well-defined for any discretization of the eigenvalue problem. In addition, as argued by Katsanoulis *et al*. [11], an approximate first integral exists in vortical regions of the flow. Since the eigenfunction H_2 approximates this first integral, we expect that the original partial differential equations also have a well-defined second-largest eigenvalue λ_2.

5. Finite-element implementation in FEniCS

We use FEniCS [17,18] to solve the eigenvalue problem described in §2. FEniCS is an open source package for finite-element analysis. The main steps of using FEniCS to solve the eigenvalue problem are as follows:

— Specify the domain Ω and create a mesh to discretize the domain. Users can use built-in functions of FEniCS to generate a mesh or load mesh files generated by other packages into FEniCS. We use a tetrahedron mesh throughout this study.

— Specify test and trial function spaces shown in (3.1). In particular, elements along with boundary conditions need to be specified to define the spaces. Here we use Lagrange elements of interpolation order r in our computations. We choose $r = 2$ unless otherwise stated.

— Specify $\mathbf{A}$ and $\mathbf{B}$ in a generalized eigenvalue problem $\mathbf{Av} = \lambda \mathbf{Bv}$. Here $\mathbf{A}$ and $\mathbf{B}$ are matrices from $a(H, h)$ and $\langle H, h \rangle$, as seen in the weak form (3.4). Since both $\mathbf{A}$ and $\mathbf{B}$ are symmetric, this problem is a generalized Hermitian eigenvalue problem.

— Call `SLEPcEigenSolver` of FEniCS to solve for the eigenvalue problem. `SLEPcEigenSolver` is a wrapper for the SLEPc eigenvalue solver [19]. It should be pointed out that we do not need to solve for all eigenvalues, only for a small subset of

them that are closest to zero. A spectral transform (shift-and-invert) is used to enhance the convergence of computing these target eigenvalues [19]. A parameter called spectral shift needs to be specified in the transform. This parameter should be close to the target eigenvalues. We set this parameter to be a negative number of small norm.

6. Benchmark studies: generalized axisymmetric flows

In this section, we construct representative streamsurfaces for generalized axisymmetric flows of the form

$$\dot{r} = u_r(r,z), \quad \dot{\theta} = u_\theta(r,z) \quad \text{and} \quad \dot{z} = u_z(r,z), \quad (r,\theta,z) \in \Omega. \tag{6.1}$$

Such flows are *generalized* axisymmetric because we also allow for a non-zero angular velocity component. In *classic* axisymmetric flow, by contrast, we have $u_\theta = 0$. We will consider a sphere, a cylinder and a hollow cylinder for the domain Ω to demonstrate the use of our methodology. By contrast, the Fourier representation used in [11] would not be able to handle these geometries.

We can find an exact first integral for any generalized axisymmetric flow as follows. For a given generalized axisymmetric flow, we have the corresponding restricted axisymmetric flow with the same u_r and u_z but zero angular velocity. The Stokes stream function $\psi(r,z)$ for the restricted axisymmetric flow is then an exact first integral. To see this, we recall that

$$u_z = \frac{1}{r}\frac{\partial \psi}{\partial r} \quad \text{and} \quad u_r = -\frac{1}{r}\frac{\partial \psi}{\partial z}. \tag{6.2}$$

We then have

$$\frac{\mathrm{d}\psi}{\mathrm{d}t} = \nabla\psi \cdot u = \frac{\partial \psi}{\partial z}\dot{z} + \frac{\partial \psi}{\partial r}\dot{r} = \frac{\partial \psi}{\partial z}u_z + \frac{\partial \psi}{\partial r}u_r \equiv 0. \tag{6.3}$$

Thus, $\psi(r,z)$ is an exact first integral, independently of the angular velocity u_θ.

We note that the generalized axisymmetric flow with (u_z, u_r) induced by the Stokes stream function $\psi(r,z)$ satisfies the continuity equation automatically by construction:

$$\nabla \cdot u = \frac{1}{r}\frac{\partial (r u_r)}{\partial r} + \frac{1}{r}\frac{\partial u_\theta}{\partial \theta} + \frac{\partial u_z}{\partial z} = \frac{1}{r}\frac{\partial (r u_r)}{\partial r} + \frac{\partial u_z}{\partial z} \equiv 0. \tag{6.4}$$

Since the existence of ψ is guaranteed, we can solve for $\psi(r,z)$ analytically provided that we have analytical expressions for $u_r(r,z)$ and $u_z(r,z)$.

In our implementation in FEniCS, we consistently use a Cartesian coordinate system for computations. So we need to transform the velocity field (6.1) to Cartesian coordinates. We have

$$u_x = \frac{\mathrm{d}(r\cos\theta)}{\mathrm{d}t} = \dot{r}\cos\theta - r\sin\theta\dot{\theta} = u_r\cos\theta - r\sin\theta u_\theta = \frac{u_r x}{\sqrt{x^2+y^2}} - y u_\theta, \tag{6.5}$$

$$u_y = \frac{\mathrm{d}(r\sin\theta)}{\mathrm{d}t} = \dot{r}\sin\theta + r\cos\theta\dot{\theta} = u_r\sin\theta + r\cos\theta u_\theta = \frac{u_r y}{\sqrt{x^2+y^2}} + x u_\theta \tag{6.6}$$

and

$$u_z = u_z(r,z). \tag{6.7}$$

As we do not impose any Dirichlet boundary conditions for the generalized flow, we have $\Omega_H = \emptyset$. Following the discussion in §4, we seek the eigenvector H_2 that corresponds to the second smallest eigenvalue λ_2. Since the existence of a non-trivial first integral is guaranteed for the generalized axisymmetric flow, we expect that the eigenvalue λ_2 is numerically close to zero. In particular, $\lambda_2 \to 0$ as the resolution of the mesh increases.

The first integral H_2 will generically not be equal to ψ because $c_1 H_2 + c_2$ is also a stationary solution to the optimization problem for all constants c_1 and c_2. However, we expect that there

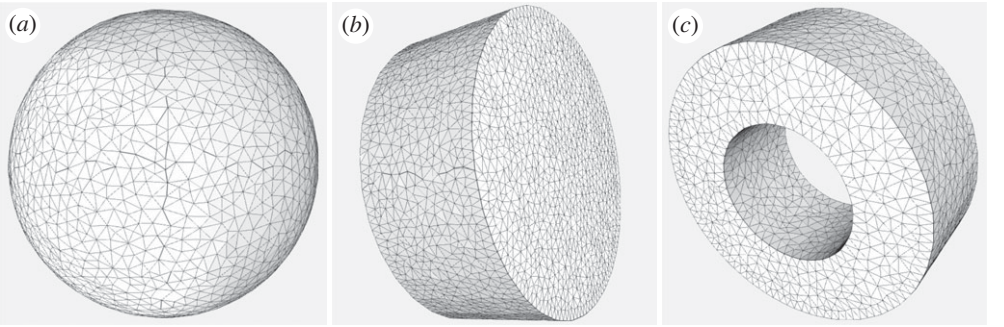

Figure 1. Meshes used in the computation of the benchmark generalized axisymmetric flows in the domain of a sphere (*a*), a cylinder (*b*) and a hollow cylinder (*c*).

exist constants c_1 and c_2 such that

$$\psi \approx c_1 H_2 + c_2 =: \hat{H}_2. \tag{6.8}$$

For the purpose of validation, we will use the least-squares method to fit these two coefficients with ψ and H_2 evaluated at a collection of grid points. We expect the coefficient of determination for the linear regression to be close to one, i.e. $R^2 \approx 1$.

(a) Spherical vortex

Let us now consider the domain $\Omega = \{(x, y, z) : x^2 + y^2 + z^2 \leq 1\}$ and

$$\dot{r} = rz, \quad \dot{z} = 1 - 2r^2 - z^2 \quad \text{and} \quad \dot{\theta} = \frac{2c}{(r^2 + \epsilon)}, \tag{6.9}$$

where c is an arbitrary constant. The flow above is a superposition of the well-known Hill's spherical vortex with a line vortex on the z axis, which induces a swirl velocity $\dot{\theta}$ [9]. We have added ϵ to avoid singularity of the swirl velocity on the z-axis. In Cartesian coordinates, we have

$$u_x = xz - \frac{2cy}{x^2 + y^2 + \epsilon}, \quad u_y = yz + \frac{2cx}{x^2 + y^2 + \epsilon} \quad \text{and} \quad u_z = 1 - 2(x^2 + y^2) - z^2. \tag{6.10}$$

The Stokes stream function for this generalized axisymmetric flow is given by

$$\psi(r, z) = 0.5r^2(1 - z^2 - r^2). \tag{6.11}$$

In the following computations, we take $c = 0.1$ and $\epsilon = 0.1$. As mentioned earlier, we use a tetrahedron mesh to discretize the sphere, as shown in figure 1*a*. We use quadratic Lagrange elements to interpolate the unknown function H. As predicted, we obtain $\lambda_1 = 0$ with a constant eigenvector. As shown in figure 2*a*, λ_2 indeed converges to zero when the number of elements is increased, indicating that the flow admits a non-trivial first integral.

As an illustration of the obtained non-trivial first integral, we plot $\hat{H}_2$ at the cross sections $x = 0$ and $z = 0$ in figure 3. Here we present the results for $\hat{H}_2$ defined in (6.8) instead of H_2 to compare against the Stokes stream function (6.11). Specifically, we first obtain H_2 discretized with 62 105 elements (see the third circle in figure 2*a*), and then fit a linear function following (6.8). Indeed, the linear relationship holds because the linear regression returns $R^2 = 0.9976$. As shown in figure 3, our numerical results match the reference solution given by (6.11) well.

We infer from figure 3 that the flow has a family of vortex rings. To illustrate this, we plot the isosurfaces for $\hat{H}_2 = 0.08$ and $\hat{H}_2 = 0.12$ in figure 4, from which we see torus-shaped isosurfaces. Given these surfaces are streamsurfaces, they should be invariant under the flow. To validate the invariance of these isosurfaces, we launch streamlines of the flow. In particular, we take a point

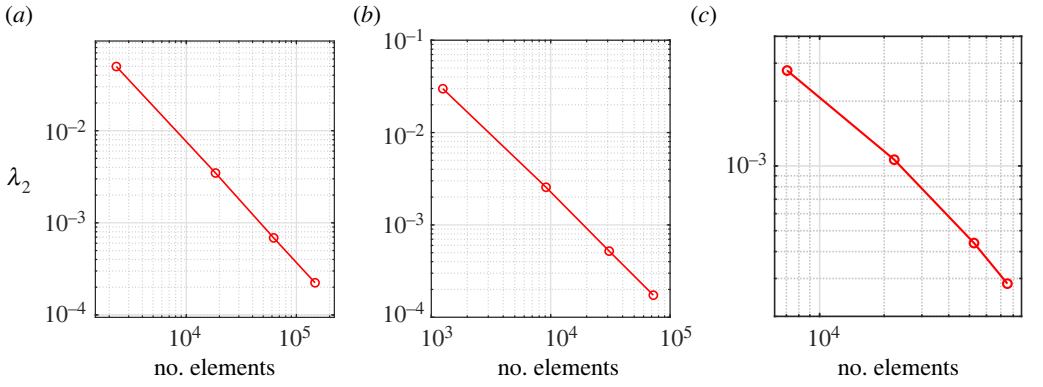

Figure 2. Second smallest eigenvalues as functions of the number of elements used in the discretization of the generalized axisymmetric flows: spherical vortex (*a*), cylindrical vortex (*b*) and Taylor–Couette flow (*c*).

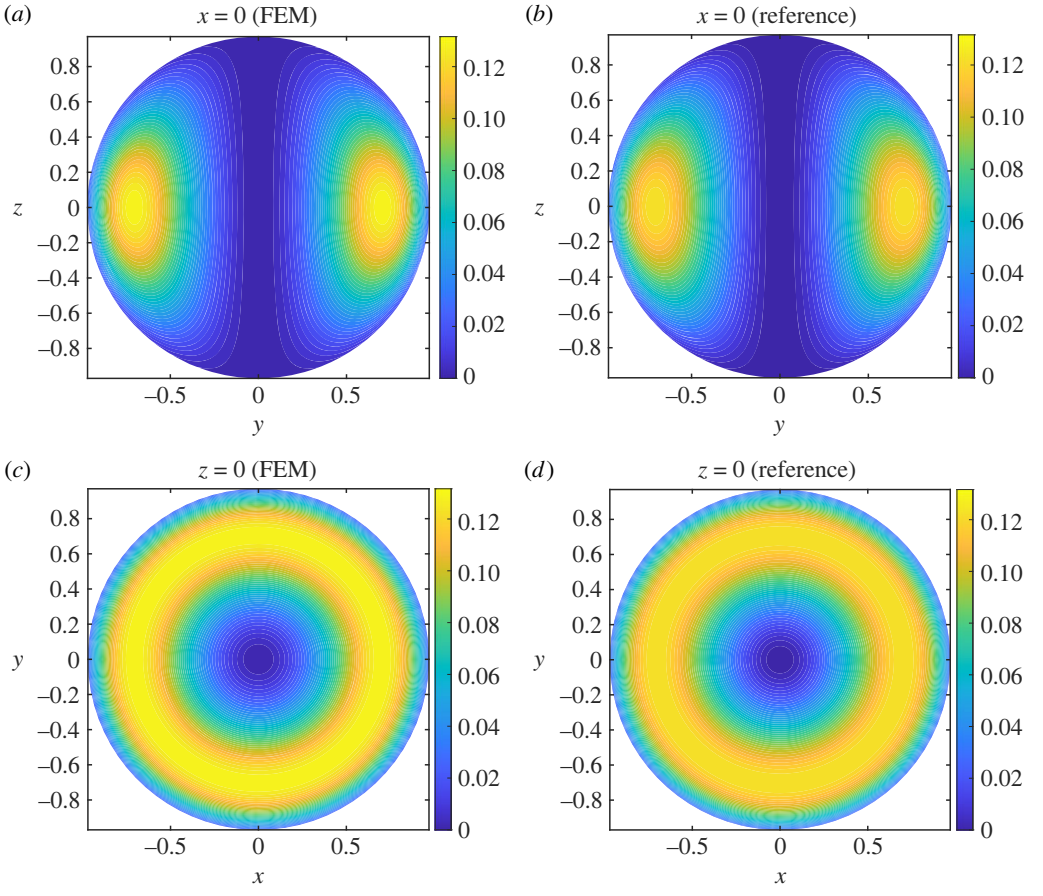

Figure 3. Contour plots of $\hat{H}_2$ for the spherical vortex obtained from finite-element methods with 62 105 elements (*a*,*c*) and ψ in (6.11) (*b*,*d*), at cross section $x = 0$ (*a*,*b*) and $z = 0$ (*c*,*d*). Here, the solutions from the finite-element computation are denoted by FEM, and that of analytical expressions are denoted by reference.

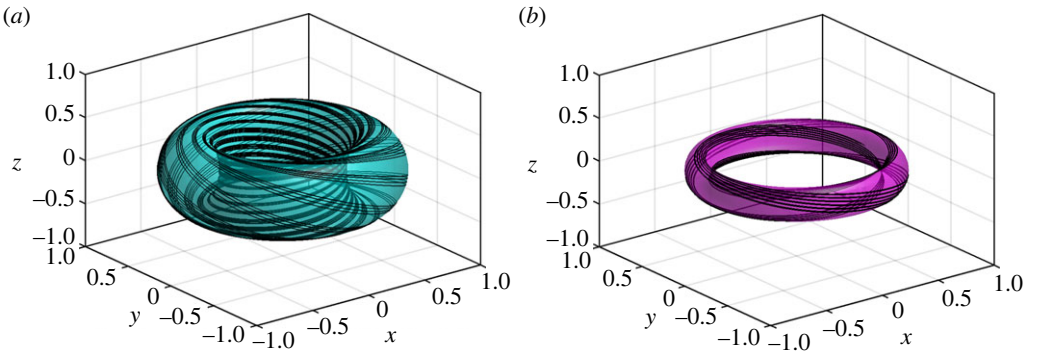

Figure 4. Contour plots of isosurfaces for $\hat{H}_2$ of the spherical vortex obtained from finite-element methods with 62 105 elements. Here we have $\hat{H}_2 = 0.08$ (*a*) and $\hat{H}_2 = 0.12$ (*b*). The black lines are streamlines from forward simulations with initial points on the isosurfaces.

on each of these isosurfaces as the initial condition and integrate the flow forward in time. The generated trajectories indeed stay on the isosurfaces, which again validates our results.

(b) Cylindrical vortex

Next, we consider the cylindrical domain $\Omega = \{(x, y, z) : x^2 + y^2 \le 1, -0.4 \le z \le 0.4\}$ and the flow

$$\dot{r} = 4rz, \quad \dot{z} = 1 - 2r^2 - 4z^2 \quad \text{and} \quad \dot{\theta} = \omega, \tag{6.12}$$

where ω denotes a rigid body angular velocity. This flow is a superposition of a cylindrical vortex with a rigid body rotation. In Cartesian coordinates, we have

$$u_x = 4xz - y\omega, \quad u_y = 4yz + x\omega \quad \text{and} \quad u_z = 1 - 2(x^2 + y^2) - 4z^2. \tag{6.13}$$

The Stokes stream function for this generalized axisymmetric flow is

$$\psi(r, z) = 0.5r^2(1 - r^2 - 4z^2). \tag{6.14}$$

One can easily check that the function above indeed induces the $\dot{r}$ and $\dot{z}$ in (6.12) (cf. (6.2)).

In the following computations, we take $\omega = 1$. We use a tetrahedron mesh to discretize the cylinder, as shown in figure 1*b*. We use quadratic Lagrange elements to interpolate the unknown function H. We again obtain $\lambda_1 = 0$ with a constant eigenvector. As shown in figure 2*b*, λ_2 converges to zero when the number of elements is increased, indicating that the flow indeed admits a non-trivial first integral.

As an illustration of the non-trivial first integral obtained in this fashion, we plot $\hat{H}_2$ at the cross sections $x = 0$ and $z = 0$ in figure 5. Similarly, we obtain $\hat{H}_2$ from H_2 via a linear fit shown in (6.8). Here H_2 is discretized with 30 888 elements. The linear fitting returns $R^2 = 0.9920$. As shown in figure 5, our numerical results closely match the reference solution given by (6.14).

We see from figure 5 that the flow has a family of vortex rings, but now these vortex rings are constrained into the cylinder instead of a sphere. We plot the isosurfaces for $\hat{H}_2 = 0.05$ and $\hat{H}_2 = 0.13$ in figure 6, from which we see torus-shaped isosurfaces. We again launch streamlines of the flow to validate the invariance of these isosurfaces. We take a point on each of these isosurfaces as the initial condition and integrate them forward in time. The generated trajectories indeed stay close to the isosurfaces, as shown in figure 6. This again serves as a validation of the results from our finite-element calculations.

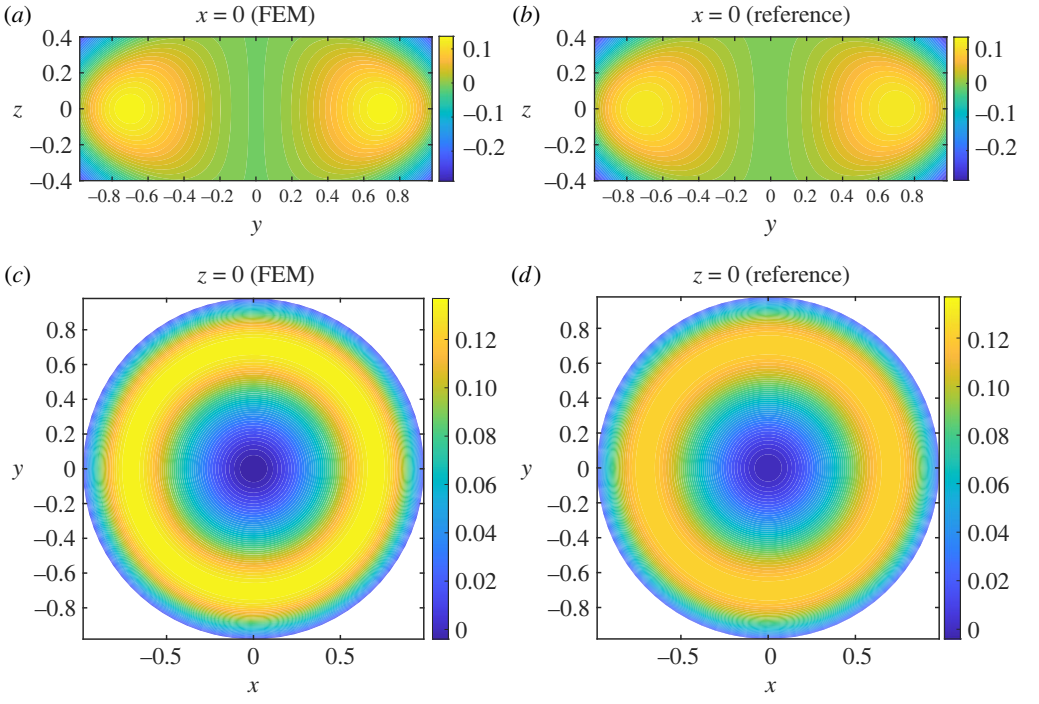

Figure 5. Contour plots of $\hat{H}_2$ for the cylindrical vortex obtained from finite-element methods with 30 888 elements (*a*,*c*) and ψ in (6.14) (*b*,*d*), at cross section $x = 0$ (*a*,*b*) and $z = 0$ (*c*,*d*). Here, the solutions from finite-element computation are denoted by FEM, and that of analytical expressions are denoted by reference.

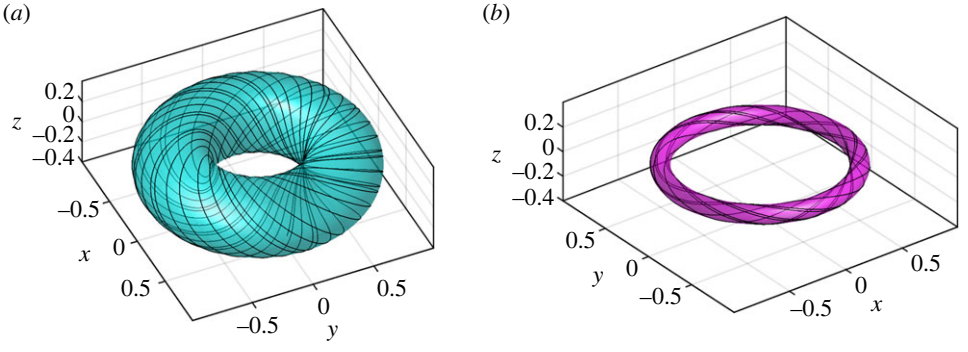

Figure 6. Contour plots of isosurfaces for $\hat{H}_2$ of the cylindrical vortex obtained from finite-element methods with 30 888 elements. Here we have $\hat{H}_2 = 0.05$ (*a*) and $\hat{H}_2 = 0.13$ (*b*). The black lines are streamlines from forward simulations with initial points on the isosurfaces.

(c) Taylor–Couette flow

We now consider a Taylor–Couette flow of a viscous fluid between two rotating cylinders. Linear stability theory successfully explains many of the flow transitions in this standard geometry [20]. For low Reynolds numbers, the flow is fully laminar and has a closed form analytic expression.

Let us consider the domain $\Omega = \{(x, y, z) : 1 \le x^2 + y^2 \le 4,\ 0 \le z \le \pi\}$, which describes the volume between two concentric cylinders with height π and radii $r_{\text{in}} = 1$, $r_{\text{out}} = 2$, respectively. We consider the case of a stationary outer wall and a steadily rotating inner wall. The steady

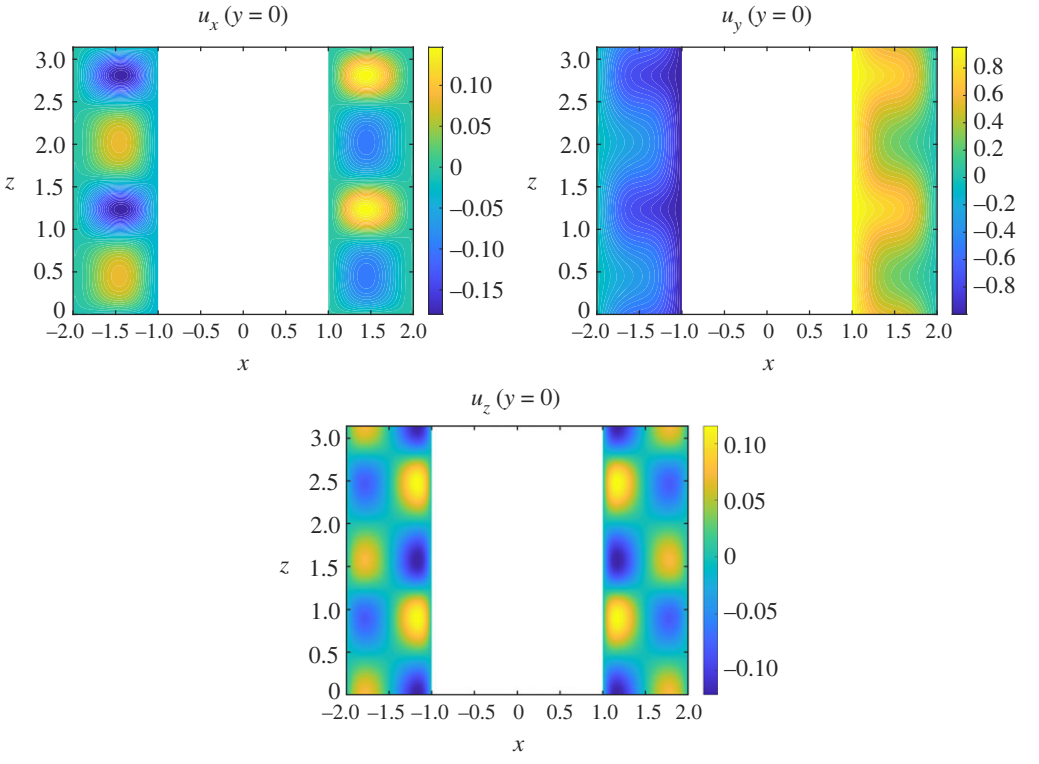

Figure 7. Contour plots of the velocity field of Taylor–Couette flow at the cross section $y = 0$.

solutions and their stability are determined by the Reynolds number defined as $\mathrm{Re} = \Omega_{\mathrm{in}} r_{\mathrm{in}} \delta/\nu$, where the radial velocity of the inner wall is Ω_{in}, the radius of the inner cylinder is r_{in}, the distance between the concentric cylinders is $\delta = r_{\mathrm{out}} - r_{\mathrm{in}}$ and the kinematic viscosity is ν. For low Reynolds numbers, the steady flow that develops is steady and purely azimuthal. Using the distance, r, from the centre line of the cylinders, the angle θ and the vertical coordinate z, the velocity field in cylindrical coordinates reads as $\mathbf{u}(r,\theta,z) = (u_r, u_\theta, u_z)(r,\theta,z)$. The base flow, which is stable for low Reynolds numbers, is called Couette flow [21] and has the form

$$u_\theta(r) = -\Omega_{\mathrm{in}} \frac{r_{\mathrm{in}}^2}{r_{\mathrm{out}}^2 - r_{\mathrm{in}}^2} r + \Omega_{\mathrm{in}} \frac{r_{\mathrm{out}}^2 r_{\mathrm{in}}^2}{r_{\mathrm{out}}^2 - r_{\mathrm{in}}^2} \frac{1}{r} \quad \text{and} \quad u_r = u_z = 0. \tag{6.15}$$

For larger Reynolds numbers, the Couette flow loses its stability and the newly obtained stable flow exhibits the well-known Taylor vortices. This flow now has non-trivial radial and axial velocities but it is still axisymmetric, that is, we have $u_r(r,z)$, $u_\theta(r,z)$ and $u_z(r,z)$, as in all the examples shown above.

This generalized axisymmetric flow is already more complicated than the previous two, as there are no analytical solutions to the Stokes stream function. As a result, we do not have analytical expressions for the velocity field in this case.

We compute this steady flow field with periodic boundary conditions for the axial direction, as it is often done in the literature [22]. This allows for a pseudo-spectral discretization via a Fourier decomposition in the z-direction and a Chebyshev decomposition in the r-direction. We use the open-source package Dedalus [23] to solve the discretized initial value problem at $\mathrm{Re} = 100$. Contours of the three components of the steady flow that develops can be seen in figure 7.

For the calculation of our approximate first integral, we restrict the domain to $z \in [0.5, 2]$ because of the periodic pattern along the z-direction, as shown in figure 7. We use a tetrahedron

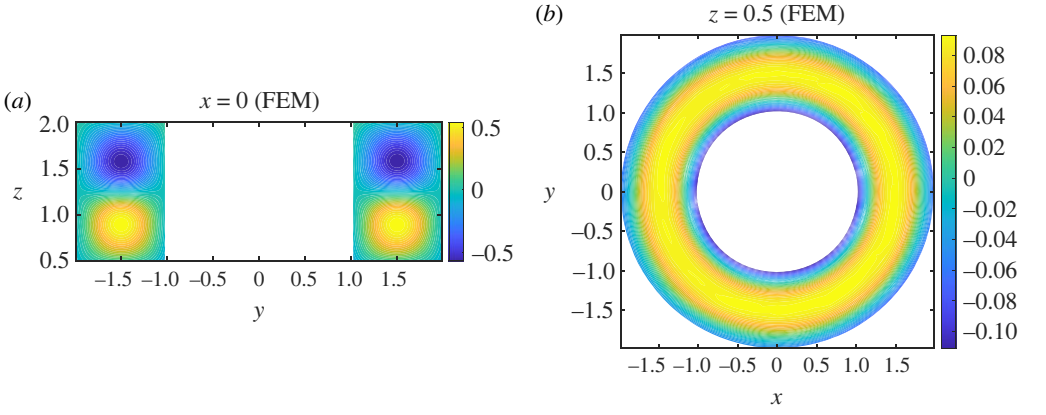

Figure 8. Contour plots of H_2 of Taylor–Couette flow obtained from finite-element methods with 52 495 elements at cross section $x = 0$ (*a*) and $z = 0.5$ (*b*).

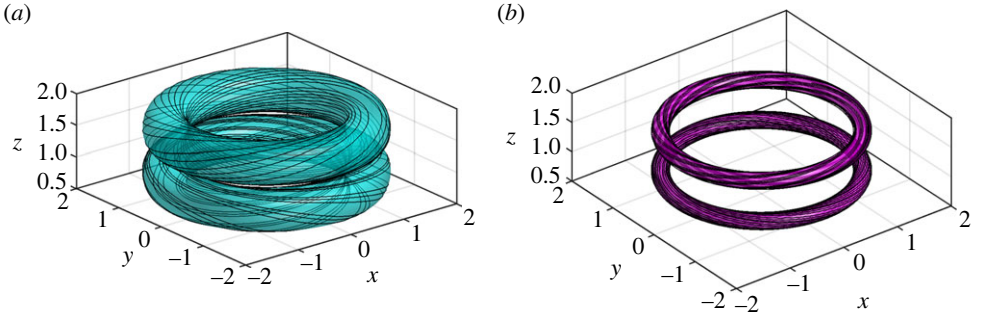

Figure 9. Contour plots of isosurfaces for $|H_2|$ of the Taylor–Couette flow obtained from finite-element methods with 52 495 elements. Here we have $|H_2| = 0.2$ (*a*) and $|H_2| = 0.5$ (*b*). The black lines are streamlines from forward simulations with initial points on the isosurfaces.

mesh to discretize the hollow cylinder, as shown in figure 1*c*. We again use quadratic Lagrange elements to interpolate the unknown function H. From figure 2*c*, we observe the monotonic decay of λ_2 with increasing number of elements. Such a decay indicates that the numerical solutions converge to the first integral we seek.

As we do not have analytical expressions for the Stokes stream function here, we simply plot H_2 instead of its linear transformation $\hat{H}_2$. The contour plots of the cross sections of H_2 obtained with 52 495 elements are shown in figure 8.

We infer from figure 8 that there are two families of vortex rings in the restricted domain, one with $H_2 > 0$ and one with $H_2 < 0$. This is consistent with the observation of Taylor vortices in experimental [20] and numerical studies [24]. We plot the isosurfaces for $|H_2| = 0.2$ and $|H_2| = 0.5$. For each case, we indeed have two vortex rings, as shown in figure 9. We launch a few streamlines with initial conditions on these surfaces. These streamlines stay close to the corresponding isosurfaces, as illustrated in figure 9.

7. Periodic flows

In this section, we consider periodic flows in the domain $\Omega = [0, 2\pi] \times [0, 2\pi] \times [0, 2\pi]$. Specifically, we will consider both the Arnold–Beltrami–Childress (ABC) [25] flow and the Euler flow [26]. The velocity field of these flows is periodic in all three directions. We note that

royalsocietypublishing.org/journal/rspa Proc. R. Soc. A 480: 20230951

periodic flows have been treated in [11], where the approximate first integral is represented by Fourier series. In the previous section, we have demonstrated the power of our finite-element computations for flows in spherical and cylindrical domains that cannot be treated via the Fourier representation. Here we illustrate that the finite-element approach can also be applied to periodic flows. Thus our finite-element implementation provides a unified treatment for both periodic and aperiodic flows. In addition, thanks to the sparsity of finite-element methods, our finite-element implementation outperforms the Fourier series schemes in [11], as we illustrate in appendix A.

For the periodic flows above, the trial function space (see (3.1)) is

$$\mathcal{H}_{\text{trial}} = \{H \in H^1(\Omega),\ H|_{x=0} = H|_{x=2\pi},\ H|_{y=0} = H|_{y=2\pi},\ H|_{z=0} = H|_{z=2\pi}\}, \tag{7.1}$$

where $H|_{x_i=a}$ denotes the evaluation of H on the plane $x_i = a$. It follows that (3.3) still holds because both H, h and $\mathbf{u}$ are periodic and

$$\mathbf{n}|_{x=0} = -\mathbf{n}|_{x=2\pi}, \quad \mathbf{n}|_{y=0} = -\mathbf{n}|_{y=2\pi} \quad \text{and} \quad \mathbf{n}|_{z=0} = -\mathbf{n}|_{z=2\pi}. \tag{7.2}$$

Indeed, the integral over the boundary of Ω vanishes (see (3.3)) because of the opposite orientation of the normal vectors on opposite faces of the cube. Therefore, the weak form (3.4) still holds and the discussions in §4 are still true.

Here we use `BoxMesh` in FEniCS to generate a mesh for Ω. Given the number of cells (N_x, N_y, N_z) in each direction, the total number of tetrahedrons is $6N_xN_yN_z$ and the total number of vertices is $(N_x+1)(N_y+1)(N_z+1)$. In the following computations, we simply set $N_x = N_y = N_z = N$ for the cubic domain. Since $\Omega_H = \emptyset$, we again have $\lambda_1 = 0$ with constant eigenvector, so we look for (λ_2, H_2).

(a) ABC flow

Consider the classic ABC flow

$$u_x = A\sin z + C\cos y, \quad u_y = B\sin x + A\cos z \quad \text{and} \quad u_z = C\sin y + B\cos x. \tag{7.3}$$

We choose $A = \sqrt{3}$, $B = \sqrt{2}$ and $C = 1$, for which the ABC flow is known to be non-integrable, i.e. there is no non-trivial exact first integral for this flow in that case [11,25].

We take $N = \{5, 10, 20, 25, 29\}$ and perform the computations with refined meshes. In figure 10*a*, we observe the monotonic decay of λ_2 as a power-law with respect to the numbers of elements. While we have observed the same decay in the previous results for the generalized axisymmetric flows, the ABC flow does not admit an exact first integral. To gain a better understanding of the behaviour of λ_2, we plot the contours of H_2 for $N = 20$ and $N = 25$ (see the third and fourth points in figure 10*a*) at cross sections $x = 0$, $y = 0$ and $z = 0$ in figure 11. By comparing subplots in the upper and lower panels, we find that both primary and secondary vortical regions are captured with $N = 20$. Here we call a vortical region 'primary' if the corresponding outermost vortex tube is of large cross-sectional area (cf. the lower-left panel of figure 12 and figure 13*a*). By contrast, we call it a secondary vortex region if the cross section of the corresponding outermost vortex tube is relatively small (cf. the upper-middle panel of figure 12 and figure 13*b*).

By contrast, when we increase N to 25, the secondary vortex structures disappear and the variation of H_2 is aggregated around the primary vortex regions. In other words, H_2 barely changes outside the primary vortical regions (see the lower panels in figure 11). So we have $\nabla H \approx 0$ outside the primary vortical regions while H converges to a first integral inside the primary vortical regions. This explains the monotonic decay of λ_2 as N increases.

As a brief summary, if we only want to extract primary vortex structures, a higher fidelity discretization is helpful. On the other hand, if we also want to extract secondary vortex structures where ∇H is of small magnitude, we should instead use a relative invariance measure

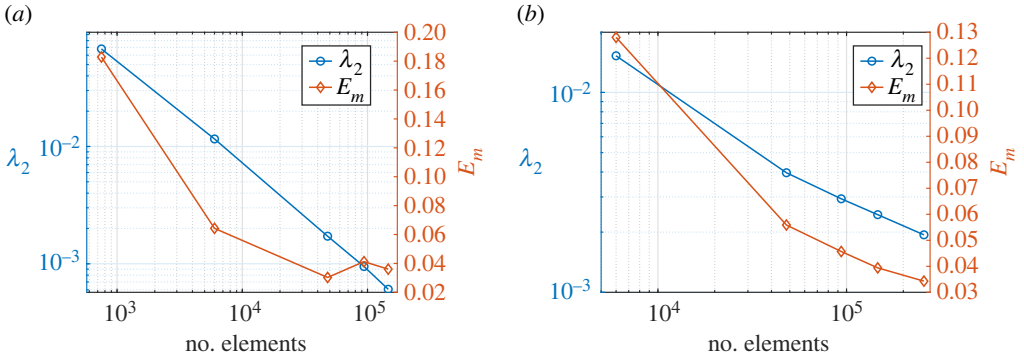

Figure 10. Second smallest eigenvalues and mean invariance errors as a function of the number of elements to discretize the periodic flows: ABC flow (*a*) and Euler flow (*b*).

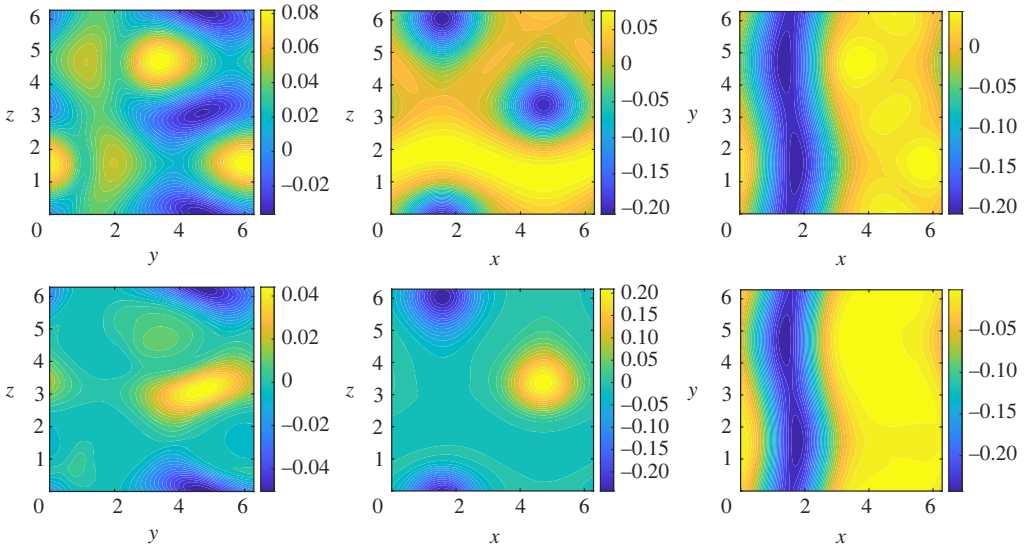

Figure 11. Contour plots of H_2 of the ABC flow at cross sections $x = 0$ (left column), $y = 0$ (middle column) and $z = 0$ (right column). Here the upper and lower rows correspond to the results with $N = 20$ (48 000 elements) and $N = 25$ (93 750 elements).

$\sqrt{\int_\Omega ((\nabla H \cdot \mathbf{u})^2/(|\nabla H|^2|\mathbf{u}|^2))\,\mathrm{d}V}$. As a variant of the above measure, we consider the mean invariance of the entire solution as an error measure [11] by defining

$$E_m = \frac{1}{m}\sum_{i=1}^{m} \frac{|\nabla H_i \cdot \mathbf{u}_i|}{|\nabla H_i| \cdot |\mathbf{u}_i|}, \tag{7.4}$$

where the summation takes place over all grid points. Here and in the example below, we take 101 grid points in each direction so that $m = 101^3$. We also plot E_m as a function of the number of elements in figure 10*a*, from which we see that E_m for $N = 20$ is the smallest among all the five cases. We attribute the observed non-monotonic decay of E_m for the ABC flow to its definition (7.4). In particular, E_m is a relative invariance measure. As shown in figure 11, H_2 becomes nearly constant when N is increased from 20 to 25 in the secondary vortex regions. Therefore, $|\nabla H_2| \approx 0$ in these regions, and then the relative error measure E_m is increased instead of decreased as N is increased from 20 to 25. This explains the observed non-monotonic decay of E_m. In short, increasing the mesh fidelity will yield smaller absolute invariance error in terms of λ_2 but may

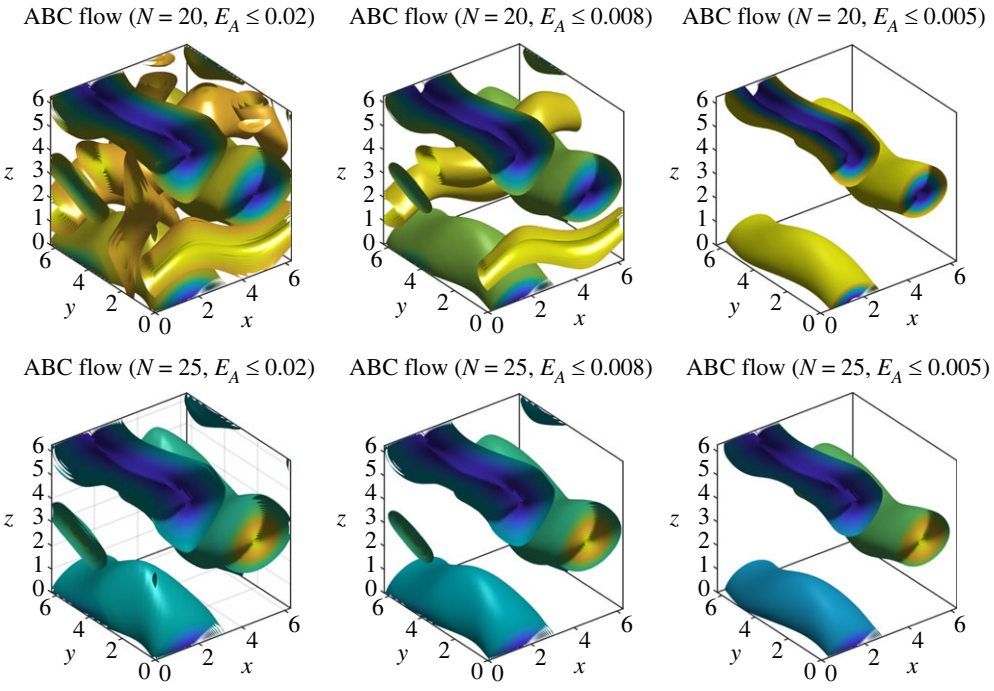

Figure 12. Isosurfaces of H_2 for the ABC flow with various filter thresholds: $E_A \le 0.02$ (left column), $E_A \le 0.008$ (middle column) and $E_A \le 0.005$ (right column). Here the upper and lower rows correspond to the results with $N = 20$ (48 000 elements) and $N = 25$ (93 750 elements).

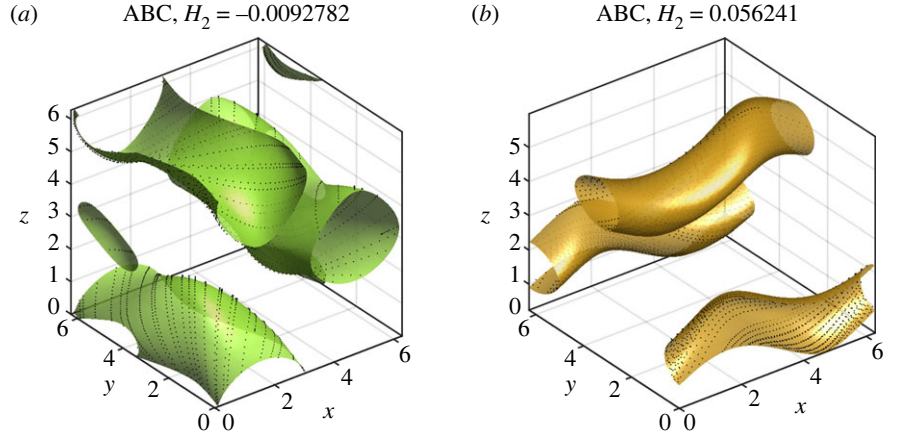

Figure 13. Contour plots of isosurfaces for H_2 of the ABC flow obtained from finite-element methods with $N = 20$ (48 000 elements). The isosurfaces in (*a*) and (*b*) panels correspond to the outermost layer of the primary and secondary vortical regions of the upper-middle panel of figure 12. Here the black dots denote simulated trajectories.

produce larger relative invariance error E_m because it tends to flatten H_2 in secondary vortex regions. Therefore, one should use E_m as an error measure to choose the proper discretization in order to obtain both primary and secondary vortex structures.

Motivated by (7.4), we introduce a filter to efficiently extract approximate streamsurfaces in vortical regions. In particular, we extract some level surfaces of H to represent the approximate

streamsurfaces. To identify whether a level surface of H is an approximate streamsurface in vortical regions, we introduce the surface-averaged invariance error [11]

$$E_A = \frac{1}{p}\sum_{i=1}^{p}\frac{|\nabla H_i \cdot \mathbf{u}_i|}{|\nabla H_i| \cdot |\mathbf{u}_i|}, \tag{7.5}$$

where p is the number of points on the surface of the level set. These points are determined by surface meshing algorithms embedded in commonly used routines, e.g. `isosurface` in MATLAB and PYTHON.

The isosurfaces of H_2 with various thresholds for E_A and different discretizations are shown in figure 12. By comparing the upper panels and corresponding lower panels (especially the first two columns), we see that the results for $N = 20$ extract both primary and secondary vortical regions while that for $N = 25$ only extract the primary vortical regions. This observation is consistent with the one we made from figure 11. From the upper panels, we also see that secondary vortical regions are filtered out when we decrease the threshold for E_A. This indicates that one can use a lower threshold to extract primary vortical regions that are robust with respect to the change of mesh fidelities.

We conclude this example by validating some of the approximate streamsurfaces we have obtained. In figure 12, we see that there are primary and secondary vortex regions. We take the outermost layers of these two regions to perform the validation. As shown in figure 13, the streamlines obtained from forward simulation stay close to the approximate streamsurfaces. The little patches in figure 13*a* are results of the periodic boundary conditions.

Such vortical structures are also commonly identified using the Q-criterion [27] or the λ_2 criterion [28]. These criteria are based on decomposing the velocity gradient ∇u as the sum of the rate-of-strain tensor ($\mathbf{S}$) and the spin tensor ($\mathbf{W}$). The functions Q and λ_2 are then introduced as heuristic measures of the strength of vortical features. Domains where $Q < 0$ or, respectively, $\lambda_2 < 0$ are then identified with regions of vortical behaviour. A streamsurface bounding the vortical region could thus be associated to the isosurface $Q = 0$ or $\lambda_2 = 0$. However, these surfaces are generally not invariant manifolds of the flow and hence do not correspond to material behaviour, even in steady flows. By contrast, the streamsurfaces obtained as isosurfaces of the approximate first integral are by construction approximately invariant manifolds of the flow. We also note that it is common to show different, non-zero Q- and λ_2-isosurfaces for flow visualization. However, as Katsanoulis *et al.* [11] show, the topology of the isosurfaces is sensitive to the choice of the isovalue. In addition, they found that expected vortical structures of the ABC flow (figure 13) could not be revealed by the λ_2-isosurfaces.

(b) Euler flow

Consider the Euler flow

$$\left.\begin{aligned} u_x &= \frac{4\sqrt{2}}{3\sqrt{3}}\left(\sin\left(x-\frac{5\pi}{6}\right)\cos\left(y-\frac{\pi}{6}\right)\sin(z)-\cos\left(z-\frac{5\pi}{6}\right)\sin\left(x-\frac{\pi}{6}\right)\sin(y)\right),\\ u_y &= \frac{4\sqrt{2}}{3\sqrt{3}}\left(\sin\left(y-\frac{5\pi}{6}\right)\cos\left(z-\frac{\pi}{6}\right)\sin(x)-\cos\left(x-\frac{5\pi}{6}\right)\sin\left(y-\frac{\pi}{6}\right)\sin(z)\right)\\ \text{and}\quad u_z &= \frac{4\sqrt{2}}{3\sqrt{3}}\left(\sin\left(z-\frac{5\pi}{6}\right)\cos\left(x-\frac{\pi}{6}\right)\sin(y)-\cos\left(y-\frac{5\pi}{6}\right)\sin\left(z-\frac{\pi}{6}\right)\sin(x)\right), \end{aligned}\right\} \tag{7.6}$$

which is also non-integrable [11,26]. We take $N = \{10, 20, 25, 29, 35\}$ and perform the computations with refined meshes. Within each cell, we use quadratic Lagrange polynomials to approximate H. In figure 10*b*, we observe the monotonic decay of λ_2 as well as the mean invariance error E_m with increasing numbers of elements. This decay indicates that more accurate results are obtained with increasing N.

The contour plots of H_2 obtained with $N = 25$ and $N = 35$ (quadratic interpolation) at the cross section $y = 0$ are presented in figure 14*a*,*b*. We infer from these two plots that there are eight

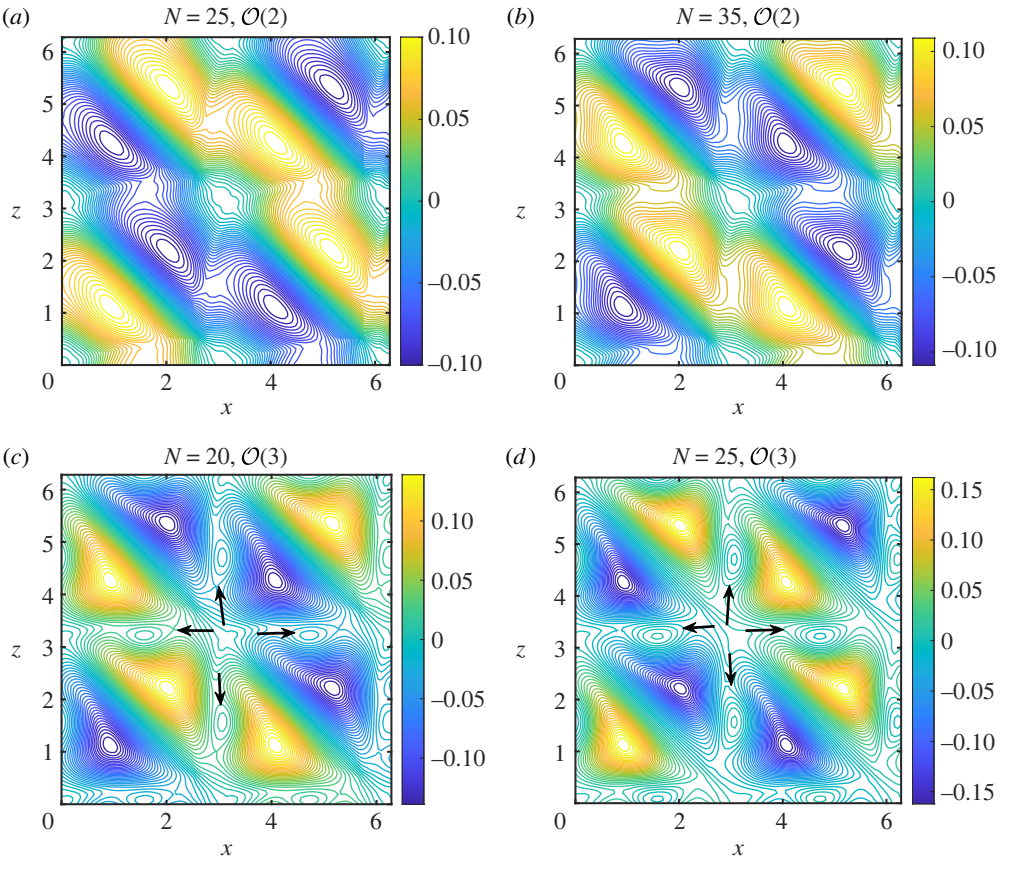

Figure 14. Contour plots of H_2 of Euler flow at cross section $y = 0$. Here H_2 is obtained with various discretizations. Here $\mathcal{O}(2)$ and $\mathcal{O}(3)$ represent quadratic and cubic interpolations for H within each cell, respectively. The number of degrees of freedom (DOF) for these four cases are 125 297 (*a*), 343 417 (*b*), 216 357 (*c*) and 422 322 (*d*).

primary vortical regions. No secondary vortical regions are observed in these two panels, which explains the monotonic decay of E_m in figure 10*b*.

To extract the approximate streamsurfaces of the eight vortex structures, we again apply the E_A-based (see (7.5)) filter. The isosurfaces of H_2 obtained with $N = 35$ (quadratic interpolation) under various thresholds for the filter are shown in figure 15. For $E_A \leq 0.05$, these isosurfaces densely fill the cube. By contrast, for $E_A \leq 0.01$, we clearly see the eight vortex tubes from the filtered isosurfaces in figure 15*b*. These tubes are entangled with each other, as shown in panel (*c*) of the figure. In panel (*c*), we also present the results from forward simulations with initial conditions on the selected approximate streamsurfaces. The trajectories obtained from forward simulation stay close to the approximate streamsurfaces, which illustrates the power of our method.

Based on a reference solution obtained from the Poincaré map [11], we know that the system also has some delicate vortical regions between the primary vortical regions. Our method is able to extract even these vortex structures by increasing the interpolation order to cubic. Indeed, as shown in figure 14*c*,*d*, delicate vortical regions are revealed and some of these small scale vortex structures are pointed out by the black arrows. These structures become more clear when we increase N from 20 to 25. Note that the numbers of DOF for the upper-right panel is more than that of the lower-left panel. This indicates that we may use higher-order interpolations to better extract delicate vortical regions.

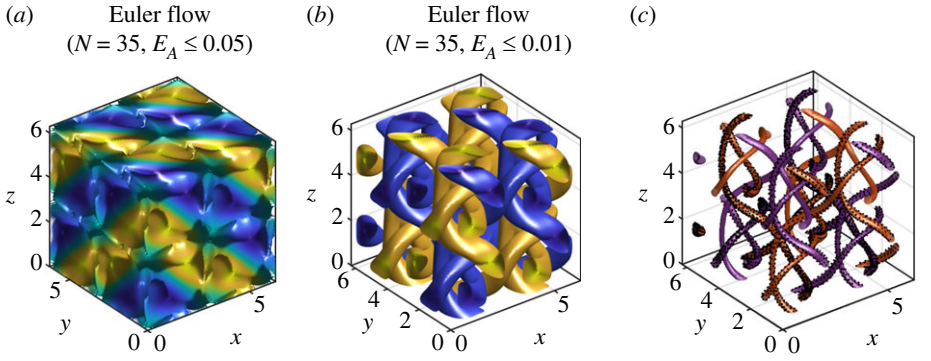

Figure 15. Isosurfaces of H_2 for the Euler flow with various filter thresholds: $E_A \leq 0.05$ (*a*) and $E_A \leq 0.01$ (*b*). Panel (*c*) gives the innermost layers of the eight vortex tubes in (*b*), along with some simulated trajectories (black dots).

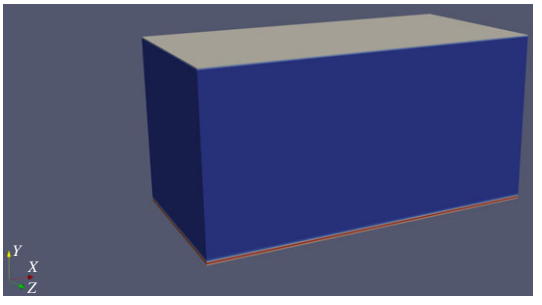

Figure 16. A schematic plot of RBC.

8. Rayleigh–Bénard convection

In this section, we consider Rayleigh–Bénard convection (RBC) in the domain $\Omega = [0, l_x] \times [0, l_y] \times [0, l_z]$. This domain is constrained by a hot plate at the bottom ($y = 0$) and a cold plate at the top ($y = l_y$), as illustrated in figure 16. In particular, the temperatures at the hot and cold plates are 274.15 K and 273.15 K, respectively. This temperature difference provides the driving force for the convection. In addition, periodic boundary conditions are imposed along the x- and z-directions. This flow is fully controlled by two dimensionless parameters. The first is the Prandtl number Pr, which describes the fluid properties as the ratio of the viscosity and the thermal diffusivity. The other parameter is the Rayleigh number Ra characterizing the strength of the thermal driving. Here we fix $Pr = 0.71$ (air at room temperature) but vary Ra to extract approximate streamsurfaces for RBC with various dynamical behaviours.

We use the computational library OpenLB [29] to simulate the RBC. OpenLB is an open-source package that provides a flexible framework for lattice Boltzmann simulations. Let the resolution of the model be N, the number of grids of the discrete model is $(N + 3) \times (2N + 3) \times (N + 3)$. More details about the simulations can be found in the `rayleighBenard3d` example of OpenLB.

Given that there are two walls where $\mathbf{u} = \mathbf{0}$, we impose $H = 0$ on the two walls. Accordingly, the trial function space (cf. (3.1)) is updated as

$$\mathcal{H}_{\text{trial}} = \{H \in H^1(\Omega),\ H|_{x=0} = H|_{x=l_x},\ H|_{y=0} = H|_{y=l_y} = 0,\ H|_{z=0} = H|_{z=l_z}\}. \tag{8.1}$$

One can easily see that (3.3) still holds with this trial function space. Consequently, the weak form (3.4) still holds and the discussions in §4 are still true.

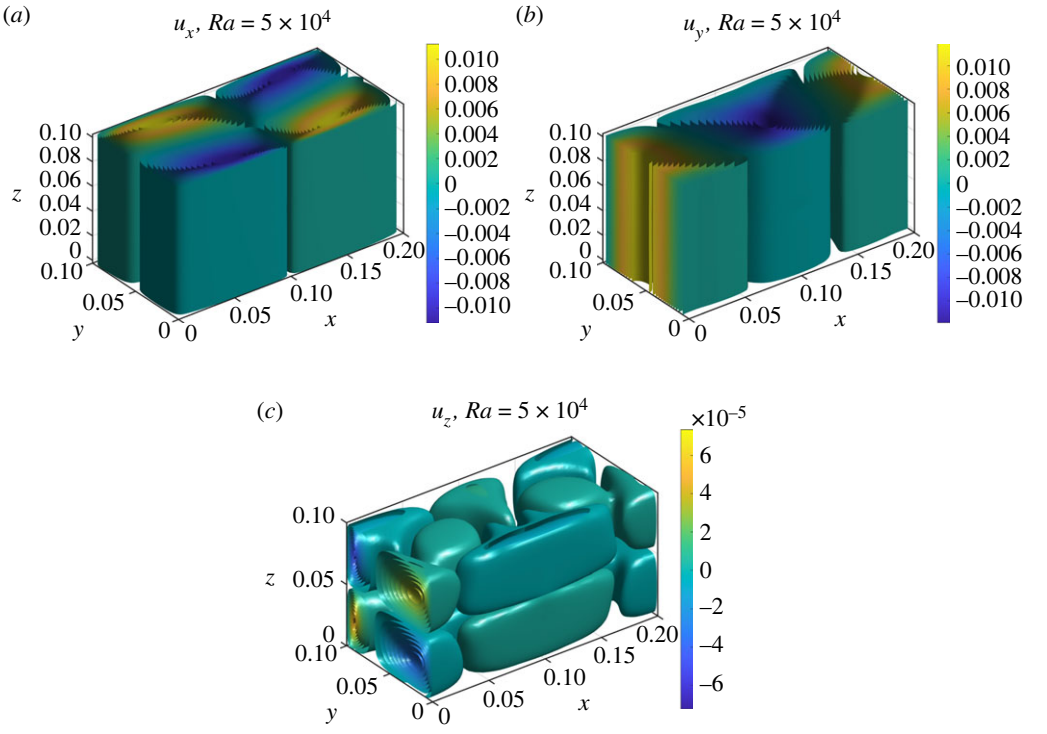

Figure 17. Isosurfaces of the velocity components of the steady state of the RBC flow with $l_x = 0.2$ m, $l_y = l_z = 0.1$ m and $Ra = 5 \times 10^4$. The (*a*), (*b*) and (*c*) panels give the results for u_x, u_y and u_z, respectively.

We again use `BoxMesh` in FEniCS to generate a mesh for Ω. Given the number of cells (N_x, N_y, N_z) in each direction, the total number of tetrahedrons is $6N_xN_yN_z$ and the total number of vertices is $(N_x + 1)(N_y + 1)(N_z + 1)$. Since $\Omega_H \neq \emptyset$, we have $\lambda_1 \neq 0$ and look for (λ_1, H_1).

(a) Quasi-two-dimensional flow

Let $l_x = 0.2$ m, $l_y = l_z = 0.1$ m and $Ra = 5 \times 10^4$, in which case the flow converges to a steady velocity field with two large-scale rolls. This motion is quasi-two-dimensional as $|u_z|$ is much smaller than $|u_x|$ and $|u_y|$, and (u_x, u_y) barely change along the z-direction, as shown in figure 17. Therefore, we expect that the flow is close to integrable, and our approach is able to extract the approximate first integral.

With $N_x = 50$ and $N_y = N_z = 25$ and quadratic interpolation, we obtain $\lambda_1 = 5.9 \times 10^{-7}$ along with a mean invariance error of $E_m = 0.02$. The isosurfaces of the corresponding H_1 are presented in figure 18. Indeed, the two primary rolls are revealed from the isosurfaces of H_1 and these isosurfaces barely change along the z-direction. To validate these results, we present the contour plot of H_1 at cross section $z = 0$ along with the streamlines of the velocity field (u_x, u_y) at the cross section in the right panel, from which we see that the streamlines match well with the contour plot.

(b) Unsteady three-dimensional flow

Next we still take $l_x = 0.2$ m, $l_y = l_z = 0.1$ m but increase the Rayleigh number to $Ra = 1 \times 10^5$. In this case, the flow converges to a limit cycle, and hence the velocity field is unsteady but periodic. We take a snapshot of the velocity field and perform the computation of the approximate first

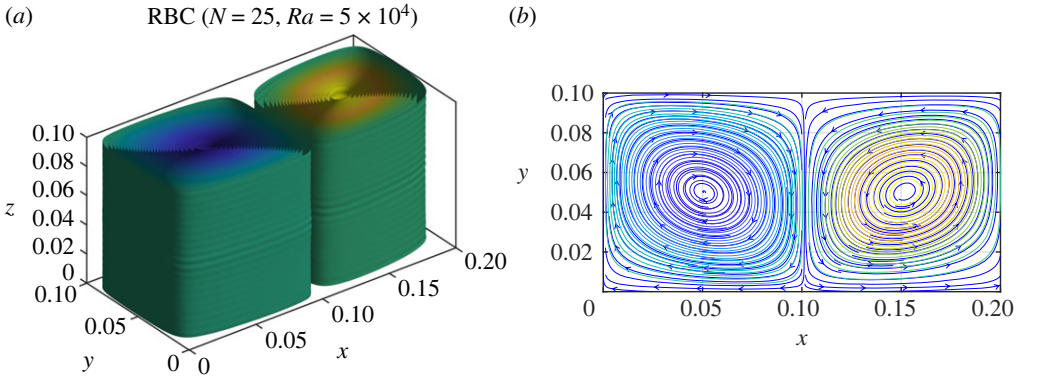

Figure 18. (*a*) Isosurfaces of H_1 for the RBC at $Ra = 5 \times 10^4$ obtained from finite-element method with $N = 25$. (*b*) Contour plot of H_1 at cross section $z = 0$, along with streamlines of (u_x, u_y) at the cross section.

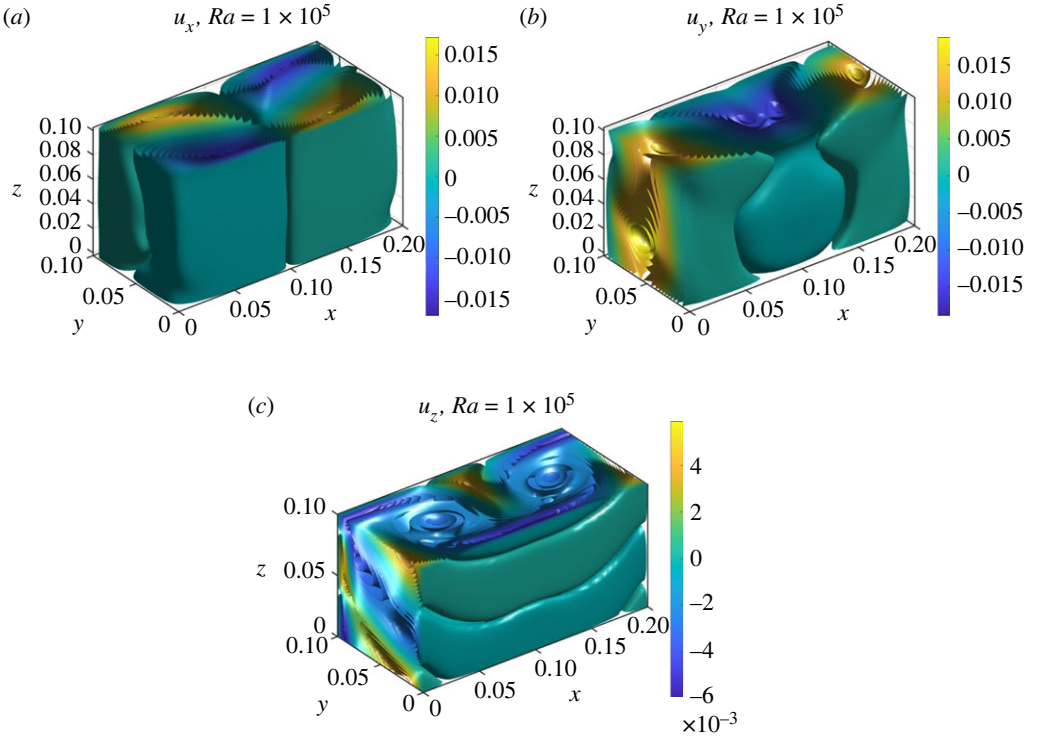

Figure 19. Isosurfaces of velocity components of a snapshot ($t = 614.519$ s) of the RBC flow with $l_x = 0.2$ m, $l_y = l_z = 0.1$ m and $Ra = 1 \times 10^5$. The (*a*), (*b*) and (*c*) panels show u_x, u_y and u_z, respectively.

integrals. The flow of this snapshot is three-dimensional, as suggested by the plots of isosurfaces of its three velocity components shown in figure 19.

With $N_x = 60$ and $N_y = N_z = 30$ and quadratic interpolation, we obtain $\lambda_1 = 5.1 \times 10^{-6}$ along with a mean invariance error of $E_m = 0.024$. The isosurfaces of the corresponding H_1 with a filter $E_A \leq 0.005$ are presented in figure 20*a*. A major vortex tube is observed for $x \geq 0.1$, while a small vortex tube exists for $x \leq 0.1$. We expect from figure 19 that there should also be a comparable vortex tube for $x \leq 0.1$ to the major one within $x \geq 0.1$. Indeed, the isosurfaces of

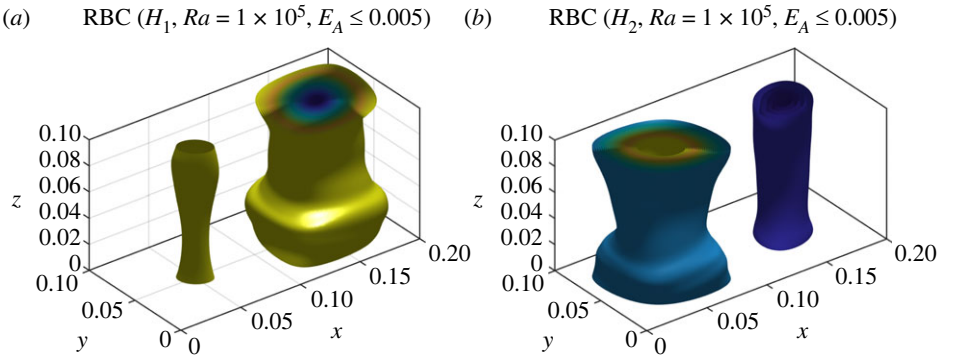

Figure 20. Isosurfaces of H_1 (*a*) and H_2 (*b*) for a snapshot of the RBC at $Ra = 1 \times 10^5$ obtained from finite-element methods with $N_x = 60$ and $N_y = N_z = 30$. Here we set a filter threshold $E_A = 0.005$.

H_2 reveal the major vortex for $x \leq 0.1$, as shown in figure 20*b*. Here we have $\lambda_2 = 6.9 \times 10^{-6}$, which is comparable to λ_1. Therefore, one may also check whether higher-order modes extract different structures than the first mode, provided that the eigenvalues of the higher-order modes are comparable to those of the first mode.

Now we launch streamlines to validate the obtained results. We take 10 random points on the outermost layer of each major vortex tube in figure 20 as initial conditions for forward simulation. Note that the extraction of the approximate first integral is an inherently Eulerian procedure. By performing the computation on a single snapshot of an unsteady flow we essentially freeze time. So, for validation, we also freeze time when we perform the time integration. As seen in figure 21*a*, *b*, these pseudo-streamlines (streamlines of the frozen flow) stay close to the extracted approximate streamsurfaces. We also launch streamlines for the unsteady flow field with the same initial conditions. As shown in figure 21*c*, *d*, the streamlines stay around the approximate streamsurfaces, which indicates that the unsteady flow field indeed admits two vortex tubes. This also indicates that the approximate stream surfaces obtained from the single snapshot of the velocity field are close to the real, time-dependent Eulerian vortex tubes.

We conclude this section with a fully three-dimensional unsteady flow in a cubic domain, where we extract vortex rings. Now we take $l_x = l_y = l_z = 0.1$ and $Ra = 1 \times 10^5$. This flow also converges to a limit cycle in steady state. We take a snapshot of the flow field and extract approximate first integrals. The contour plots of velocity components for this snapshot are shown in figure 22, which show that it is indeed a three-dimensional flow.

With $N_x = 60$, $N_y = N_z = 30$ and quadratic Lagrange elements, we obtain $\lambda_1 = 3.9 \times 10^{-5}$ along with mean invariance error $E_m = 0.03$. By decreasing the filter threshold E_A, we are able to extract two vortex rings, as shown in figure 23*c*. These vortex rings are different from the vortex tubes that we extracted before.

Repeating the procedure used to produce figure 21, we obtain results shown in figure 24. The obtained pseudo-streamlines stay close to the extracted approximate streamsurfaces, and the streamlines of the unsteady flow field also stay around the approximate streamsurfaces, indicating the persistence of the vortex rings.

(c) Momentum transport barriers

Recently, Haller *et al*. [15] formalized the notion of a barrier to the transport of active vectorial quantities, such as the linear momentum or vorticity. For example, barriers to the transport of linear momentum can be understood as surfaces that have a net-zero transport of linear momentum through them. In [15], it is shown that such barriers are best defined as structurally stable invariant manifolds of an associated barrier-equation derived from the Navier–Stokes

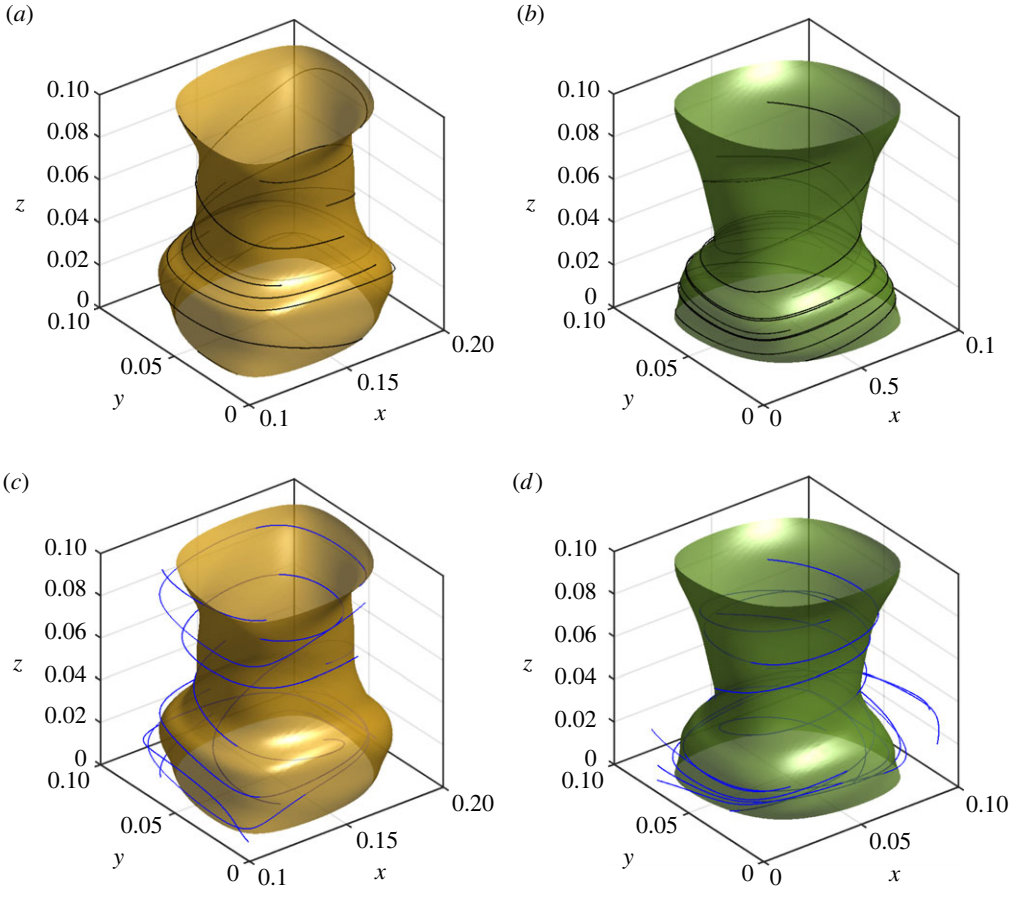

Figure 21. Outermost isosurfaces of the two major vortex tubes in figure 20, along with streamlines of 10 randomly selected points in each of the surface. Trajectories from the forward simulations of the *frozen* vector field are plotted with black lines and shown in (*a*) and (*b*). By contrast, the blue lines in (*c*) and (*d*) denote streamlines of the unsteady flow started from the same initial points. Here the forward simulation time is 20 s since $|\mathbf{u}| \sim \mathcal{O}(0.01)$ m s^{-1}.

equations. It is also important to note that [15] defines transport barriers as material structures, which need to satisfy the requirement of objectivity (also known as frame-indifference) [30]. The objective structures extracted from the barrier-equation have also been compared with other Lagrangian and Eulerian coherent structures in [16,31]. For a recent review, we refer to [32]. We recall that instantaneous momentum transport barriers of a velocity field $\mathbf{u}(\mathbf{x}, t)$ at time t can be identified as streamsurfaces of the barrier equation

$$\mathbf{x}'(s) = \Delta\mathbf{u}(\mathbf{x}(s), t), \tag{8.2}$$

where s denotes a parameterization of streamlines forming the streamsurfaces. We will apply our FEM-based approach to the extract approximate streamsurfaces of the barrier field.

The flow near the top and bottom plates is contained in thin boundary layers. As a result $\Delta\mathbf{u}$ within the boundary layers has a much larger magnitude than outside the boundary layers. Consequently, the solution H will also exhibit boundary layers: H is nearly constant outside the boundary layers given $\Delta\mathbf{u}$ is negligible, while ∇H is orthogonal to $\Delta\mathbf{u}$ inside the boundary layers. We are mainly interested in vortical structures outside the boundary layers because

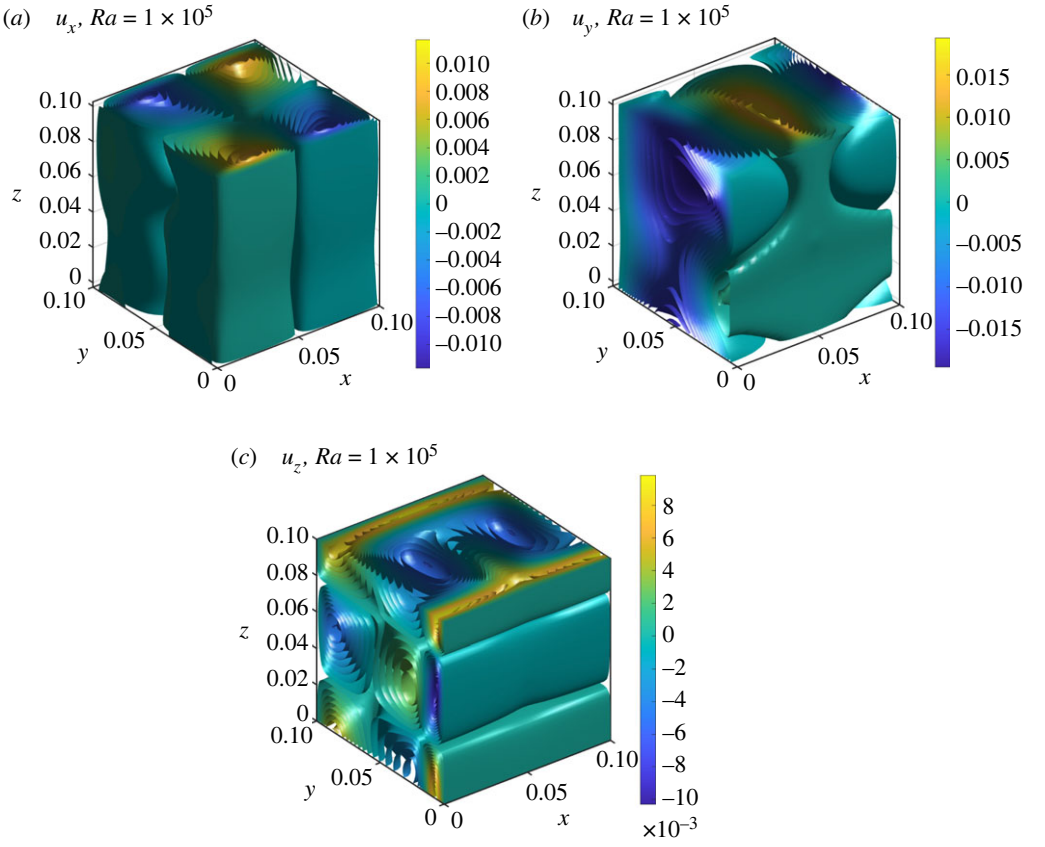

Figure 22. Isosurfaces of the velocity components of a snapshot ($t = 619.515$ s) of the RBC flow with $l_x = l_y = l_z = 0.1$ and $Ra = 1 \times 10^5$. The (*a*), (*b*) and (*c*) panels show u_x, u_y and u_z, respectively.

those boundary layers are very thin. To extract vortical structures outside boundary layers, we normalize the active velocity field as [16]

$$\mathbf{x}'(s) = \frac{\Delta\mathbf{u}(\mathbf{x}(s), t)}{|\Delta\mathbf{u}(\mathbf{x}(s), t)|}. \tag{8.3}$$

(i) Quasi-two-dimensional flow

We first consider the steady quasi-two-dimensional flow discussed in §a. We compute the Laplacian $\Delta\mathbf{u}$ at grid points using second-order finite difference [33]. With $N_x = 60$, $N_y = N_z = 30$ and quadratic interpolation, we obtain $\lambda_1 = 0.3420$ and $\lambda_2 = 0.5806$. With the filter (7.5) applied, we obtain the isosurfaces for H_1 in figure 25 (the first two rows), from which we see that the extracted barriers consist of a tube in the right half ($x \geq 0.1$) of the domain. We expect that there is another tube in the left half ($x \leq 0.1$) of the domain. Indeed, the isosurfaces for H_2 reveal the other tube, as shown in the last two rows in figure 25.

Next we launch streamlines on the outermost layers of the two tubes in the last column of figure 25. When the integration time is not too long, the obtained trajectories stay close to the extracted approximate streamsurfaces, as seen in the left column of figure 26. However, given the streamsurfaces are not necessarily attracting, these trajectories may drift far away from the surfaces for longer time integration, as seen in the second and third columns of figure 26, where panels in the third column are the projections of panels in the middle column onto the (x, y) plane. We note that the drifted flow is nearly contained in the extracted barriers. Interestingly,

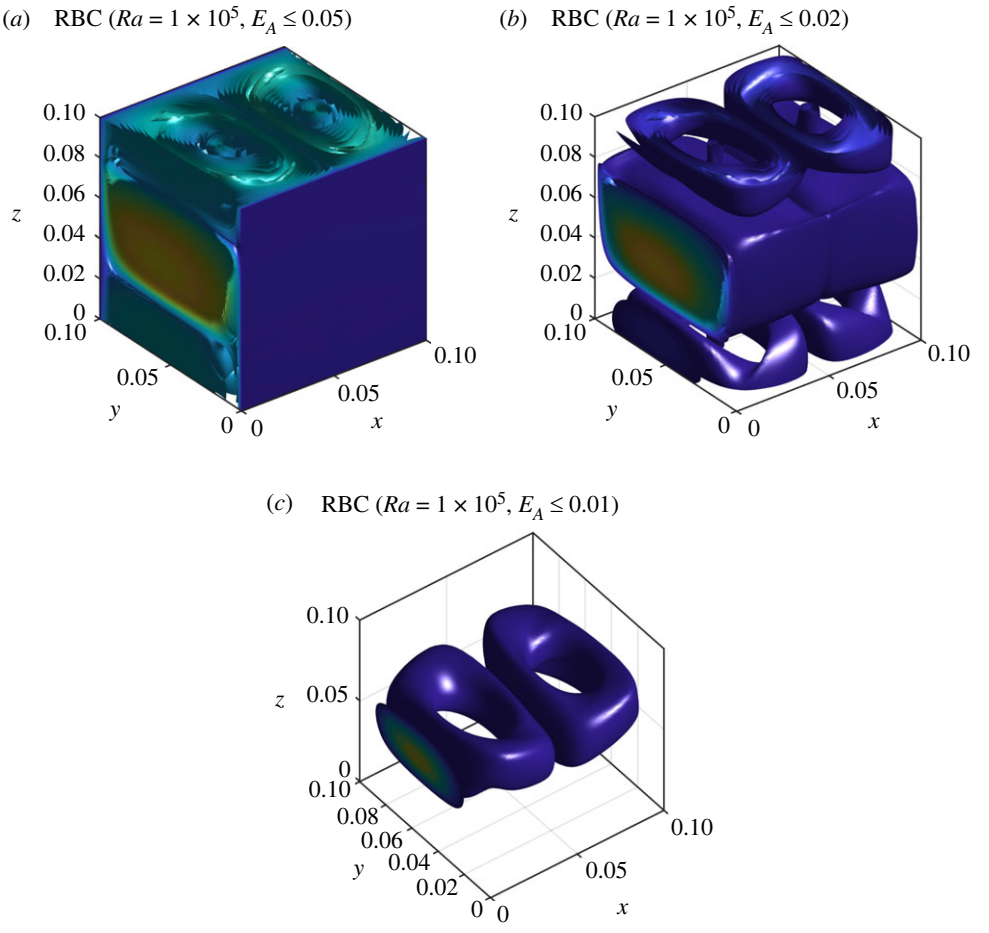

Figure 23. Isosurfaces of H_1 for the RBC flow in a cube with various filter thresholds: $E_A \leq 0.05$ (*a*), $E_A \leq 0.02$ (*b*) and $E_A \leq 0.01$ (*c*).

the two panels in the third column are similar to the two projected plots in the middle column of figure 25. This again validates the obtained results. To further identify structures of the simulated trajectories, we present the intersection points of these trajectories along with a Poincaré section $y = 0.05$. As seen in the last column, there exists invariant tori inside the vortex tube for $x \leq 0.1$.

(ii) Three-dimensional flow

Now we extract momentum barriers of the flow snapshot shown in figure 20. This is a snapshot of an unsteady three-dimensional flow. With $N_x = 60$, $N_y = N_z = 30$, we obtain $\lambda_1 = \lambda_2 = \lambda_3 = 1$ and $\lambda_4 = 19.2$. The first three modes correspond to boundary layer modes, while the last one gives structures outside the boundary layer. As an illustration of the boundary layer modes, we present the contour plot of H_1 at the cross section $z = 0$ in figure 27*a*. We see from the left panel that H_1 is barely changing outside the boundary layers. By contrast, the contour plot of H_4 at $z = 0$ in the right panel of the figure reveals structures outside the boundary layers. So, we should look for H_4. Note that λ_4 is large, which indicates that the barrier field does not admit any globally defined first integral. However, we can still apply the filter (7.5) to extract approximate streamsurfaces.

Isosurfaces of H_4 with different filter thresholds are plotted in figure 28. By decreasing the threshold properly, we are able to extract two disconnected tubes shown in the right panel of the

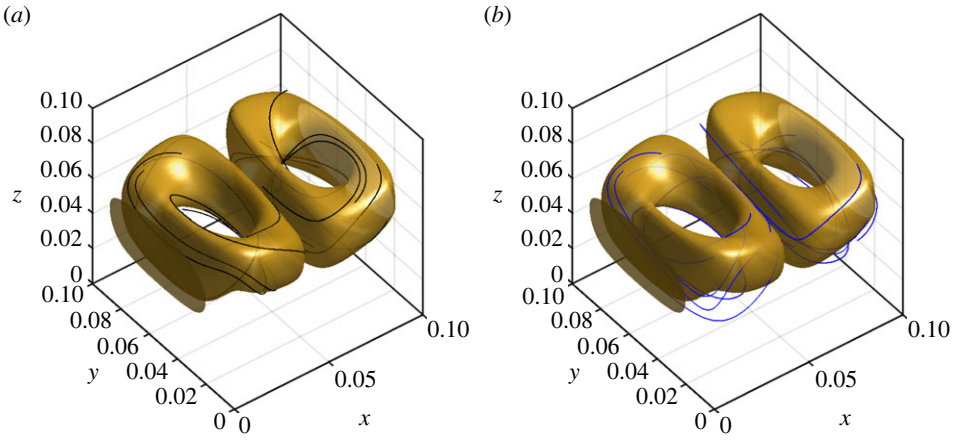

Figure 24. Outermost isosurfaces of the two major vortex rings in figure 23, along with streamlines of 10 randomly selected points in each surface. Trajectories of the forward simulations of the *frozen* vector field are plotted in black lines and shown in panel (*a*). The blue lines in panel (*b*) denote streamlines of the unsteady flow started from the same initial points. Here the forward simulation time is 20 s, since $|\mathbf{u}| \sim \mathcal{O}(0.01)$ m s^{-1}.

figure. To validate the obtained approximate streamsurfaces, we launch streamlines started from five randomly selected points on the outermost layers of each of the two tubes in the right panel of figure 28. Here we set the integration time to be 0.1 s given that the velocity magnitude is of order 1 while the characteristic length scale for the tubes is of order 0.1 m. As seen in figure 29, the trajectories from numerical integration stay close to the extracted streamsurfaces.

9. Conclusion

We have established a variational method for the construction of tubular and toroidal streamsurfaces for three-dimensional flow visualization. This method is an extension of the Fourier series expansion proposed in [11] from spatially periodic domains to general spatial domains. We have formulated an optimization problem seeking the closest first integrals. The isosurfaces of these closest first integrals give approximate streamsurfaces in vortical regions of three-dimensional flows. We have derived the first-order necessary conditions to the optimal solution that gave rise to an eigenvalue problem of a set of linear partial differential equations. We have used finite-element methods to solve the eigenvalue problem. Although we did not carry out a formal analysis of the spectrum of the partial differential equations, numerical evidence based on the discretized problem suggests that the eigenvalue problem we have posed is well defined.

We have demonstrated the effectiveness of the proposed variational construction through a suite of examples. We started from simple benchmark studies including spherical and cylindrical vortex flows as well as Taylor–Couette flow to illustrate that the finite-element based implementation can handle flows in domains with arbitrary geometries. We have also applied the method to periodic flows such as ABC flows and Euler flows to show that this method also works well for periodic flows. Finally, we have considered Rayleigh–Bénard convection flows to demonstrate the effectiveness of the proposed method for more complicated flows.

We have used regular mesh grids in the computations of this study. It is instructive to implement an adaptive mesh to enhance the performance of our variational construction. In particular, we can use the distribution of invariance error to conduct the adaptive change of the mesh. This adaptation could play an important role in extracting tubular and toroidal streamsurfaces in complicated three-dimensional flows, especially for turbulent flows.

We have implemented our variational construction using FEniCS. However, the variational method proposed here is generic and can be implemented in other finite-element packages

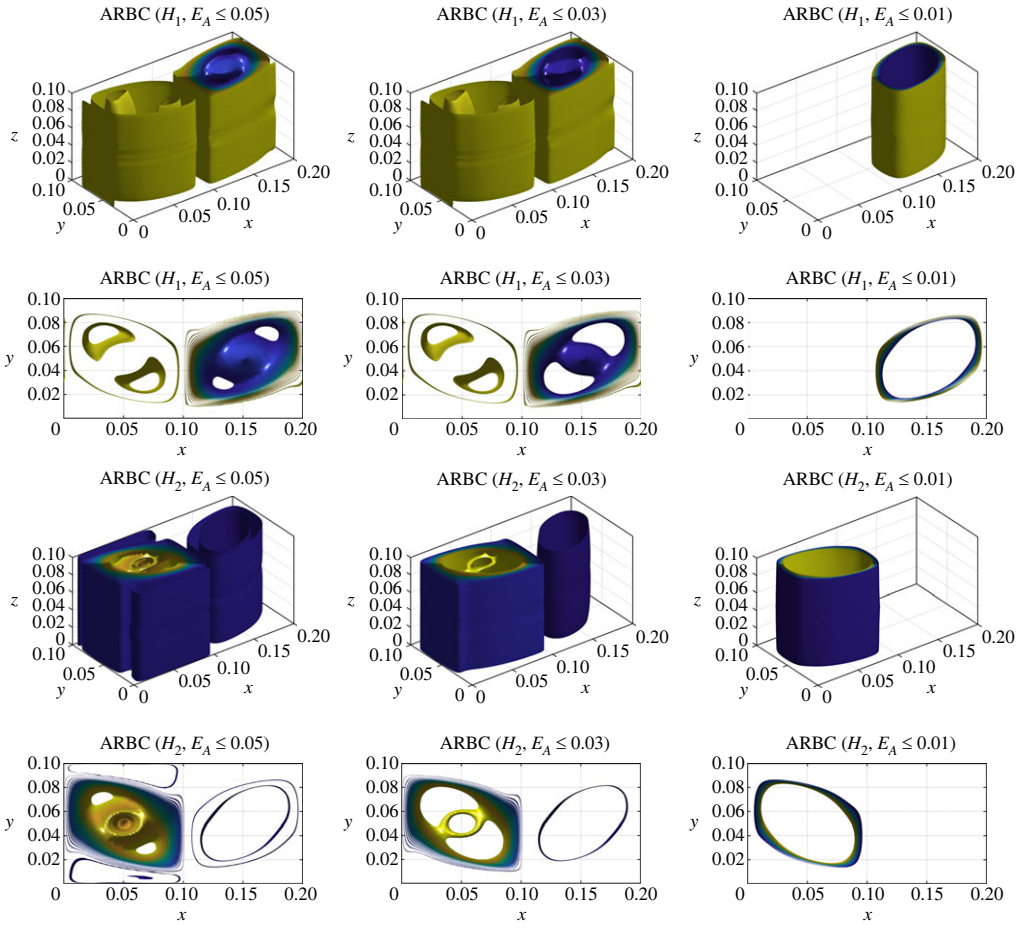

Figure 25. Barriers to momentum transport in the RBC flow at $Ra = 5 \times 10^4$ shown as isosurfaces of the approximate first integral. Here the results are based on various filter thresholds applied to H_1 (the first two rows) and H_2 (the last two rows). The panels in the second/fourth row are the projection of the panels in the first/third row onto (x, y) plane.

or more specialized codes. In particular, advanced eigensolvers that support high-performance computing can be used to speed up the computation of eigensolutions.

Data accessibility. The code and data used to generate the numerical results included in this paper are available from the GitHub repository: https://github.com/mingwu-li/first_integral [34].

Declaration of AI use. We have not used AI-assisted technologies in creating this article.

Authors' contributions. M.L.: formal analysis, investigation, methodology, software, validation, visualization, writing—original draft, writing—review and editing; B.K.: investigation, methodology, writing—review and editing; G.H.: conceptualization, project administration, supervision, writing—review and editing.

All authors gave final approval for publication and agreed to be held accountable for the work performed therein.

Conflict of interest declaration. We declare we have no competing interests.

Funding. We received no funding for this study.

Appendix A

We compare the performance of our finite-element implementation against the Fourier series approach [11] for the two periodic flows in §7. We use the error metric E_m defined in (7.4) to

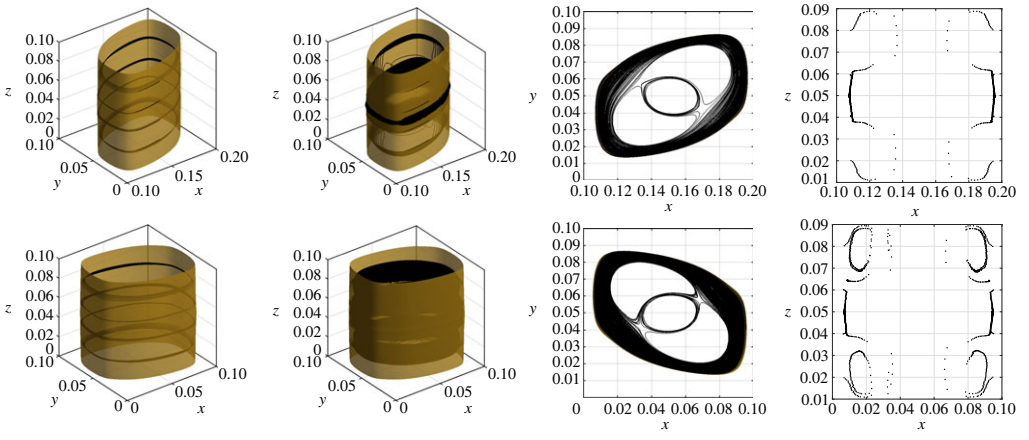

Figure 26. Outermost isosurfaces of the two major vortex tubes in figure 20*b*, along with streamlines of four selected points in each of the surfaces. Trajectories from the forward simulations of active vector field are plotted in black lines. The integration time for the first and second columns is 2 s and 50 s. The third column gives the projection of the panels in the middle plane onto (x, y) plane, while the last column gives the intersection points of the simulated trajectories with the Poincaré section $y = 0.05$ m.

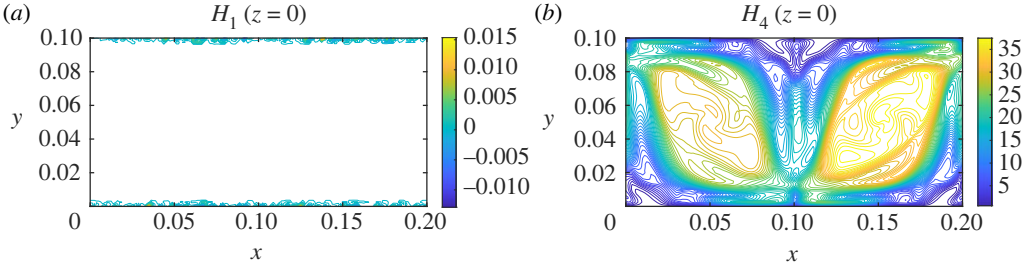

Figure 27. Contour plots of (*a*) H_1 and (*b*) H_4 of the active vector field of a snapshot of the RBC flow with $Ra = 1 \times 10^5$ at cross section $z = 0$ (see figure 19 for the snapshot).

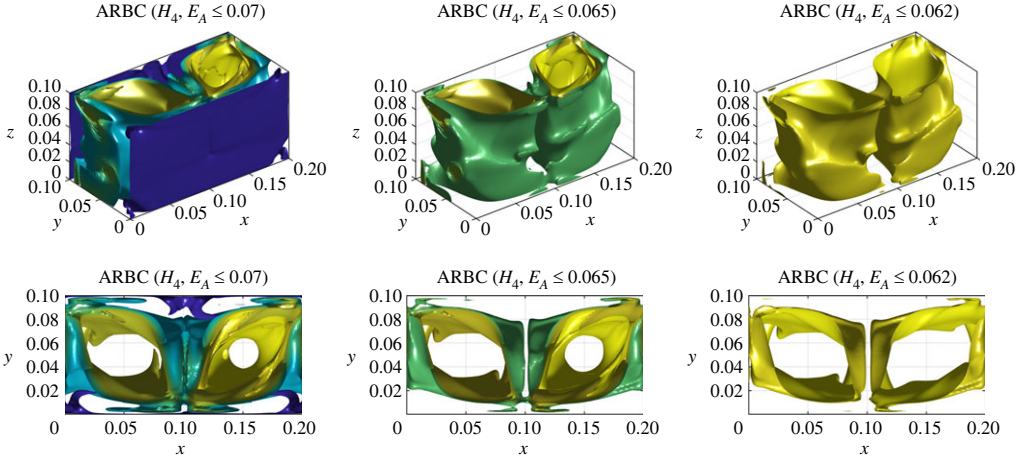

Figure 28. Isosurfaces of H_4 for the active vector field of a snapshot of the RBC flow with $Ra = 1 \times 10^5$ (see figure 27*b*) with various filter thresholds: $E_A \leq 0.07$ (left panels), $E_A \leq 0.065$ (middle panels) and $E_A \leq 0.062$ (right panels). The lower panels are the projections of the upper panels onto (x, y) plane.

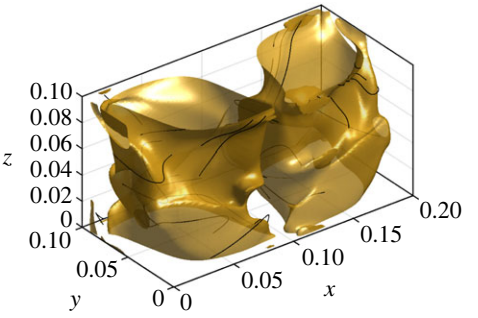

Figure 29. Outermost isosurfaces of the two tubes in the right panel of figure 28, along with streamlines initialized from five randomly selected points on the surfaces.

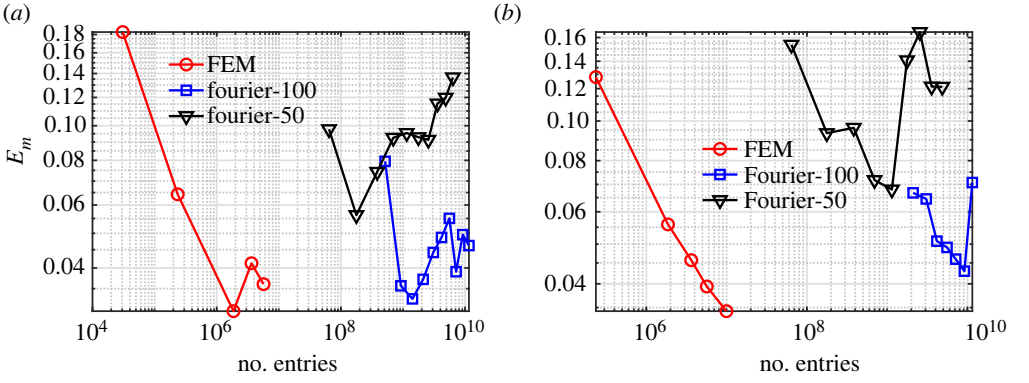

Figure 30. Mean invariance error E_m as a function of the number of entries (dN_{DOF} for the finite-element method and mN_{mode} for the Fourier series scheme) for ABC flow (*a*) and Euler flow (*b*) in §7. Here the legends 'Fourier-100' and 'Fourier-50' represent $m = 100^3$ and $m = 50^3$, respectively.

make comparisons. This metric E_m gives the averaged normalized invariance error evaluated at a collection of grid points.

We recall that our finite-element implementation seeks the leading eigenvalue of a generalized eigenvalue problem. As seen in §5, the matrices **A** and **B** of the generalized eigenvalue problem are of size $N_{DOF} \times N_{DOF}$, where N_{DOF} denotes the number of degrees-of-freedom (DOF) of the finite-element discretization. In the Fourier approach [11], one seeks the leading singular value of a matrix $\mathbf{C} \in \mathbb{C}^{m \times N_{mode}}$. Here, N_{mode} is the number of Fourier modes and m is the number of grid points.

We infer from the size and sparsity of the matrices **A**, **B**, **C** that the Fourier approach requires much more memory than that of our finite-element implementation. Indeed, the number of non-zero entries of the matrices **A** and **B** is dN_{DOF} because the two matrices are sparse. Here d is the bandwidth of the two matrices. We found that $d \approx 29$ when we use Lagrange elements of interpolation order two. On the contrary, the number of entries in the full matrix **C** is mN_{mode}. In [11], $m = 100^3$ was used and hence N_{mode} often was restricted to be less than 10^4. Indeed, we found that for $N_{mode} = 1.7 \times 10^4$, the memory required to compute the leading singular value has exceeded 200 GB. Since $m = 100^3 \gg d \approx 29$, the finite-element method requires much less memory than the Fourier approach for the same degree of fidelity, i.e. when $N_{mode} = N_{DOF}$.

We plot the metric E_m against the number of non-zero entries, that is, dN_{DOF} or mN_{mode}, to compare the performance of the two schemes. Indeed, the computational cost of leading eigenvalues or singular values is also directly related to these numbers of entries. As shown in figure 30, in order to achieve the same level of error metric E_m, the number of entries needed for

the finite-element method is much smaller than for the Fourier approach in both two periodic flows. In addition, the finite-element method can achieve smaller errors with an increasing number of entries. Therefore, the finite-element implementation shows better scaling. We have performed Fourier-based computations with both $m = 100^3$ and $m = 50^3$, since decreasing the number of gridpoints allows us to use a Fourier series with higher number of modes. However, we have found that increasing the number of gridpoints, m, is more beneficial in terms of the error metric E_m.

References

1. Van Wijk JJ. 1993 Implicit stream surfaces. In *Proc. Visualization '93, San Jose, CA, 25–29 October*, pp. 245–252. IEEE.
2. Born S, Wiebel A, Friedrich J, Scheuermann G, Bartz D. 2010 Illustrative stream surfaces. *IEEE Trans. Vis. Comput. Graph.* **16**, 1329–1338. (doi:10.1109/TVCG.2010.166)
3. Schulze M, Esturo JM, Günther T, Rössl C, Seidel H-P, Weinkauf T, Theisel H. 2014 Sets of globally optimal stream surfaces for flow visualization. *Computer Graphics Forum* **33**, 1–10. (doi:10.1111/cgf.12356)
4. Hultquist JP. 1992 Constructing stream surfaces in steady 3D vector fields. In *Proc. Visualization '92, Boston, MA, 19–23 October*, pp. 171–178. IEEE.
5. Yang Y, Pullin DI. 2010 On lagrangian and vortex-surface fields for flows with Taylor–Green and Kida–Pelz initial conditions. *J. Fluid Mech.* **661**, 446–481. (doi:10.1017/S0022112010003125)
6. Yang Y, Pullin D. 2011 Evolution of vortex-surface fields in viscous Taylor–Green and Kida–Pelz flows. *J. Fluid Mech.* **685**, 146–164. (doi:10.1017/jfm.2011.287)
7. Xiong S, Yang Y. 2017 The boundary-constraint method for constructing vortex-surface fields. *J. Comput. Phys.* **339**, 31–45. (doi:10.1016/j.jcp.2017.03.013)
8. Arnold VI, Khesin BA. 2021 *Topological methods in hydrodynamics*, vol. 125. Berlin, Germany: Springer Nature.
9. Haller G, Mezic I. 1998 Reduction of three-dimensional, volume-preserving flows with symmetry. *Nonlinearity* **11**, 319–339. (doi:10.1088/0951-7715/11/2/008)
10. He P, Yang Y. 2016 Construction of initial vortex-surface fields and clebsch potentials for flows with high-symmetry using first integrals. *Phys. Fluids* **28**, 037101. (doi:10.1063/1.4943368)
11. Katsanoulis S, Kogelbauer F, Shankar Kaundinya R, Ault J, Haller G. 2022 Approximate streamsurfaces for flow visualization. *J. Fluid Mech.* **954**, A28. (doi:10.1017/jfm.2022.992)
12. Cheng CQ, Sun YS. 1989 Existence of invariant tori in three-dimensional measure-preserving mappings. *Celestial Mech. Dyn. Astron.* **47**, 275–292. (doi:10.1007/BF00053456)
13. Pöschel J. 1982 The concept of integrability on cantor sets for hamiltonian systems. *Celestial Mech.* **28**, 133–139. (doi:10.1007/BF01230665)
14. Peikert R, Sadlo F. 2009 Topologically relevant stream surfaces for flow visualization. In *Proc. of the 25th Spring Conf. on Computer Graphics, Budmerice, Slovakia, 23–25 April*, pp. 35–42. New York, NY: Association for Computing Machinery.
15. Haller G, Katsanoulis S, Holzner M, Frohnapfel B, Gatti D. 2020 Objective barriers to the transport of dynamically active vector fields. *J. Fluid Mech.* **905**, A17. (doi:10.1017/jfm.2020.737)
16. Aksamit NO, Haller G. 2022 Objective momentum barriers in wall turbulence. *J. Fluid Mech.* **941**, A3. (doi:10.1017/jfm.2022.316)
17. Alnæs M *et al.* 2015 The fenics project version 1.5. *Arch. Numer. Softw.* **3**, 9–23.
18. Logg A, Mardal K-A, Wells G. 2012 *Automated solution of differential equations by the finite element method: the FEniCS book*, vol. **84**. Berlin, Germany: Springer Science & Business Media.
19. Hernandez V, Roman JE, Vidal V. 2005 SLEPc: a scalable and flexible toolkit for the solution of eigenvalue problems. *ACM Trans. Math. Softw.* **31**, 351–362. (doi:10.1145/1089014.1089019)
20. Gollub JP, Swinney HL. 1975 Onset of turbulence in a rotating fluid. *Phys. Rev. Lett.* **35**, 927–930. (doi:10.1103/PhysRevLett.35.927)
21. Landau LD, Lifshitz EM. 1987 *Fluid mechanics*. Oxford, UK: Pergamon.
22. Shi L, Hof B, Rampp M, Avila M. 2017 Hydrodynamic turbulence in quasi-keplerian rotating flows. *Phys. Fluids* **29**, 044107. (doi:10.1063/1.4981525)
23. Burns KJ, Vasil GM, Oishi JS, Lecoanet D, Brown BP. 2020 Dedalus: a flexible framework for numerical simulations with spectral methods. *Phys. Rev. Res.* **2**, 023068. (doi:10.1103/PhysRevResearch.2.023068)

24. Barenghi CF. 1991 Computations of transitions and taylor vortices in temporally modulated Taylor–Couette flow. *J. Comput. Phys.* **95**, 175–194. (doi:10.1016/0021-9991(91)90258-M)
25. Dombre T, Frisch U, Greene JM, Hénon M, Mehr A, Soward AM. 1986 Chaotic streamlines in the abc flows. *J. Fluid Mech.* **167**, 353–391. (doi:10.1017/S0022112086002859)
26. Antuono M. 2020 Tri-periodic fully three-dimensional analytic solutions for the Navier–Stokes equations. *J. Fluid Mech.* **890**, A23. (doi:10.1017/jfm.2020.126)
27. Hunt J, Wray A, Moin P. 1988 Eddies, streams, and convergence zones in turbulent flows. ctr-s88, Center for Turbulence Research.
28. Jeong J, Hussain F. 1995 On the identification of a vortex. *J. Fluid Mech.* **285**, 69–94. (doi:10.1017/S0022112095000462)
29. Krause MJ *et al.* 2021 Openlb—open source lattice Boltzmann code. *Comput. Math. Appl.* **81**, 258–288. (doi:10.1016/j.camwa.2020.04.033)
30. Truesdell C, Noll W. 2004 *The non-linear field theories of mechanics*. Berlin, Germany: Springer.
31. Aksamit NO, Hartmann R, Lohse D, Haller G. 2023 Interplay between advective, diffusive and active barriers in (rotating) Rayleigh–Bénard flow. *J. Fluid Mech.* **969**, A27. (doi:10.1017/jfm.2023.563)
32. Haller G. 2023 *Transport barriers and coherent structures in flow data: advective, diffusive, stochastic, and active methods*. Cambridge, UK: Cambridge University Press.
33. Baer M. 2018 Findiff software package. See https://github.com/maroba/findiff.
34. Li M, Kaszás B, Haller G. 2024 Variational construction of tubular and toroidal streamsurfaces for flow visualization. GitHub repository. (https://github.com/mingwu-li/first_integral)